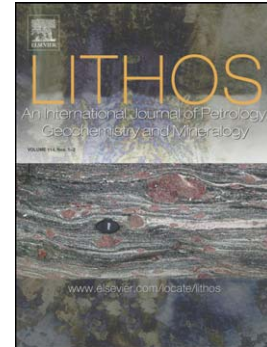# Accepted Manuscript

Cocos Plate Seamounts offshore NW Costa Rica and SW Nicaragua: Implications for large-scale distribution of Galápagos plume material in the upper mantle

Antje Herbrich, Kaj Hoernle, Reinhard Werner, Folkmar Hauff, Paul v.d. Boogard, Dieter Garbe-Schönberg

Please cite this article as: Herbrich, Antje, Hoernle, Kaj, Werner, Reinhard, Hauff, Folkmar, Boogard, Paul v.d., Garbe-Schönberg, Dieter, Cocos Plate Seamounts offshore NW Costa Rica and SW Nicaragua: Implications for large-scale distribution of Galápagos plume material in the upper mantle, *LITHOS* (2014), doi: 10.1016/j.lithos.2014.10.014

This is a PDF file of an unedited manuscript that has been accepted for publication. As a service to our customers we are providing this early version of the manuscript. The manuscript will undergo copyediting, typesetting, and review of the resulting proof before it is published in its final form. Please note that during the production process errors may be discovered which could affect the content, and all legal disclaimers that apply to the journal pertain.

Cocos Plate Seamounts offshore NW Costa Rica and SW Nicaragua: Implications for large-scale distribution of Galápagos plume material in the upper mantle

Antje Herbrich[1*], Kaj Hoernle[1], Reinhard Werner[1], Folkmar Hauff[1], Paul v.d. Boogard[1], Dieter Garbe-Schönberg[2]

[1] GEOMAR Helmholtz Centre for Ocean Research Kiel, Wischhofstraße 1-3, D-24148 Kiel, Germany

[2] Institute of Geosciences, University of Kiel, Ludewig-Meyn-Strasse 10, D-24118 Kiel, Germany

Abstract

The origin of intraplate volcanism not directly part of a hotspot track, such as diffuse seamount provinces, and the extent of mantle plume influence on the upper mantle remain enigmatic. Here we present new $^{40}Ar/^{39}Ar$ age data and geochemical (major and trace-element and Sr-Nd-Pb isotopic) data from seamounts on the Cocos Plate presently located offshore of NW Costa Rica and SW Nicaragua. The seamounts (~7-24 Ma) require mixing of an enriched ocean island basalt composition, similar to that of the Northern Galápagos Domain, with two depleted components. One of the depleted components is similar to East Pacific Rise normal mid-ocean ridge basalt and the other has more depleted incompatible elements, either reflecting secondary melting of MORB or a depleted Galápagos plume component. Seamounts with ages significantly younger than the ocean crust formed in an intraplate setting and can be explained by northward transport of Galápagos plume material along the base of the Cocos Plate up to 900 km away from the hotspot and 250-500 km north of the Galápagos hotspot track. We propose that melting occurs due to decompression as the mantle upwells to shallower depth as it

flows northwards, either due to changes in lithospheric thickness or as a result of upwelling at the edge of a viscous plug of accumulated plume material at the base of the lithosphere. The tholeiitic to alkaline basalt compositions of the Cocos Plate Seamounts compared to the more silica under-saturated compositions of Hawaiian rejuvenated and arch (alkali basalts to nephelinites) lavas is likely to reflect the significant difference in age (<25 vs ~90 Ma) and thus thickness of the lithosphere on which the lavas were erupted.

1. Introduction

Although many studies have been carried out to investigate the interaction of hotspots or mantle plumes with a nearby oceanic spreading center (e.g. Geldmacher et al., 2013; Ingle et al., 2010; Ito and Lin, 1995; Kincaid et al., 1995; Kincaid et al., 1996; Ribe, 1996; Schilling et al., 2003), the extent to which the plume material spreads out along the base of the lithosphere away from the ridge has not been established. At Hawaii, located on old (90 Ma), thick lithosphere, the presence of a 1 km high and ~1,000 km wide bathymetric swell around the active volcanic islands, however, indicates that the proposed underlying mantle plume affects a much larger portion of the upper mantle (e.g. Phipps Morgan et al., 1995). This influence is reflected by young alkaline volcanism along the edge of the swell, leading to the formation of rejuvenated volcanism on Hawaiian Volcanoes and the Hawaiian Arch volcanic fields up to 400 km north and south of the plume center presumably beneath the Big Island of Hawaii (e.g. Clague et al., 1990; Clague et al., 2002; Frey et al., 2000; Lipman et al., 1989).

About 21 of the proposed 30 to 50 hot spots on Earth are, however, located near mid-ocean ridges and interact with young, thin lithosphere, resulting in geomorphological and geochemical anomalies along the spreading axes (e.g.Christie

et al., 2005; Detrick et al., 2002; Ito et al., 2003; Sinton et al., 2003). While plume material can influence nearby ridges for distances of up to 1,000 km along-axis (Schilling et al., 1976; Schilling et al., 1982; Vogt, 1976), the extent to which plume material that a) does not flow into the ridge system spreads laterally along the base of the lithosphere away from the ridge axis and b) affects the chemical composition of the upper mantle (asthenosphere and possibly lithosphere) is still poorly constrained.

The Galápagos hotspot with the adjacent Cocos-Nazca or Galápagos Spreading Center (GSC) is a classic location to study interaction between a plume and young, thin lithosphere near a spreading center, representing the opposite endmember to the extensively studied Hawaiian system (intraplate hotspot interacting with old, thick lithosphere). Although many studies have investigated the interaction between the Galápagos plume and the GSC and East Pacific Rise (EPR) (e.g. Bowles et al., 2014; Christie et al., 2005; Detrick et al., 2002; Geldmacher et al., 2013; Ingle et al., 2010; Kokfelt et al., 2005; Schilling et al., 2003; Schilling et al., 1982; Sinton et al., 2003), the extent to which the plume spreads out along the base of the lithosphere away from the ridge and causes intraplate volcanism has not been established.

Depending on the relative position of the GSC to the Galápagos plume, two distinct aseismic hotspot tracks have formed – the Cocos Ridge on the Cocos Plate and Carnegie Ridge on the Nazca Plate (Fig. 1; e.g. Hey, 1977; Holden and Dietz, 1972; Werner et al., 2003; Wilson and Hey, 1995). The hotspot track on the Cocos Plate also consists of a Seamount Province on the northwestern side of the Cocos Ridge (von Huene et al., 1995). Systematic variations in basalt chemistry along the GSC are explained by transport of Galápagos plume material to and then along the spreading center (Christie et al., 2005; Detrick et al., 2002; Ingle et al., 2010; Kokfelt et al., 2005; Pedersen and Furnes, 2001; Schilling et al., 2003; Schilling et al., 1976),

but today's influence of the hotspot can only be detected as far as 99.5 °W, ~1,000 km from the Galápagos Islands (Schilling et al., 2003). Geldmacher et al. (2013) proposed that Galápagos plume material reached the main EPR ridge system (currently located 1,100 km west of the Galápagos) during times of superfast EPR spreading (22.5-11 Ma ago), possibly by increased "ridge suction" forces, and thus affected the formation of the Cocos Plate crust that was formed along the EPR during this time interval.

A number of observations support transport of Galápagos plume material beneath the Cocos Plate. Off the coast of Costa Rica, drill cores from ODP-Leg 170 (Fig. 1a) contained sills with Galápagos-type geochemical compositions (<16 Ma; Sadofsky et al., 2009 and references therein) intruded into Cocos Plate crust that is between 22.1 and 24.1 Ma old (Barckhausen et al., 2001). In addition, unusual young lavas occur within the Cocos and Carnegie Ridge hotspot tracks (O'Connor et al., 2007), which also contain the geochemical characteristics of magmas from the Galápagos plume (Harpp et al., 2005; Werner et al., 2003), but not necessarily in accordance with the geochemical composition of the surrounding, older hotspot track volcanic rocks. Hence the significantly younger age of these intraplate volcanic rocks that have Galápagos-type compositions may reflect active plume outflow over several hundreds of kilometers, consistent with low seismic velocities within the upper asthenosphere beneath the Cocos Hotspot track (O'Connor et al., 2007).

We sampled 19 dispersed seamounts located 800-1,300 km away from the presumed plume center at Fernandina, and 250-500 km north of the morphological hotspot track (Cocos Ridge) during R/V Sonne cruise SO208 "PLUMEFLUX" in July 2010. Out major goal was to determine if these seamounts show any evidence for the involvement of Galápagos plume material, in order to constrain further the distribution of Galápagos plume material in the upper mantle and to elucidate the

origin of these seamounts, referred to as Cocos Plate Seamounts (CPS; Fig. 1). Here we present ^{40}Ar/^{39}Ar age data from 9 and geochemistry of all sampled CPS in order to unravel the origin of this intraplate volcanism. We show that a) these seamounts formed both on- and off-axis of the EPR and b) that flow of Galápagos Northern Domain plume material both along the GSC and EPR and also along the base of the lithosphere can explain the intraplate seamount volcanism up to 900 km away from the hotspot.

2. Regional Background

The Galápagos Archipelago thought to be the surface expression of a long-lived mantle plume (e.g. Duncan and Hargraves, 1984; Morgan, 1971), originating from the earth's lower mantle (Graham et al., 1993; Montelli et al., 2006). It is spatially zoned in geochemistry with lavas with radiogenic Sr and Pb and unradiogenic Nd isotope ratios erupting in a horseshoe-shaped region surrounding an area where the volcanic products reflect an isotopically depleted composition, similar to N-MORB (e.g. Geist et al., 1988; Harpp and White, 2001; White et al., 1993) or depleted plume material (Hoernle et al., 2000). Based on the isotopic composition of the erupted lavas, the "horseshoe" has been subdivided into three distinct enriched geographic domains – Northern (containing Wolf, Darwin and Pinta Islands), Central (including Fernandina) and Southern (including Floreana) Galápagos Domains (Geldmacher et al., 2003; Hoernle et al., 2000; Werner et al., 2003). The Central Domain, however, may represent a mixture of Southern and Northern Domains plus depleted material (Hoernle et al., 2000). Therefore the Galápagos hotspot could either reflect an asymmetrically zoned plume with three (Hoernle et al., 2000) or two compositional endmembers (Rohde et al., 2013), forming vertical stripes or filaments in the plume conduit (Farnetani and Hofmann, 2009; Lohmann et al., 2009).

The Nazca and Cocos Plates formed due to the break up of the Farallon Plate, which was most likely caused by a fracture zone passing over the Galápagos hotspot ~23 Ma ago (Lonsdale, 2005; Lonsdale and Klitgord, 1978). The north-south-trending East Pacific Rise borderes the Cocos Plate in the west and the east-west-trending Galápagos Spreading Center borders it in the south. In the east, the Cocos Plate subducts along the Central American Trench with convergence rates varying between 85-88 mm/a (DeMets et al., 1990).

A rough-smooth boundary (RSB; ~2-5 km width; see dashed line in Fig. 1) separates the smoother crust that forms at the EPR in the north from the rough seafloor that forms at the GSC in the south (Fisher et al., 2003). The Cocos Ridge and Seamount Province are located on the crust formed at the GSC and are geochemically zoned at their older end similar to the Galápagos Archipelago (Harpp et al., 2005; Hoernle et al., 2000; Werner et al., 2003). The Cocos Plate that formed at the EPR contains abundant large, randomly distributed seamounts, including the study area (shown in box in Fig. 1a) located ~250-500 km northwest of the Cocos Ridge. The CPS, covering <5 % of the seafloor, are located at depths of 1,500 to 3,800 m below sea level (b.s.l.). They reach elevations of up to 2,000 m above the surrounding seafloor and have diameters of up to 10-14 km. Absence of signs of sea surface erosion point to formation beneath sea level.

The morphology of the CPS ranges from irregular- to cone-shaped edifices. Close to the Central American Trench, they have been dissected by faults related to the bending of the subducting Cocos Plate. Some, mainly circular shaped seamounts with ~4 km diameter at their base, are characterized by central craters, which are located between 3,500 and 3,800 m b.s.l. A representative selection of CPS bathymetry is provided in the electronic appendices (Fig. A1). Highly vesicular volcaniclastic samples containing particles, such as "Limu o Pele" (thin flakes of

volcanic glass formed when magma bubbles burst), are strong indicators for explosive fragmentation of the erupted lavas at great water depths.

3. Sample preparation

Fresh volcanic glass was chipped off on board of the ship and further processed at GEOMAR (Kiel, Germany). The glass chips were wrapped in tubular film and paper and carefully crushed with a hammer. Manganese crusts and altered rims were cut off from whole-rock samples, which were then crushed into smaller pieces using a jaw crusher. Both volcanic glass and whole-rock fragments were sieved preserving the fractions between 250 μm and 2 mm and repeatedly washed with de-ionized water in an ultrasonic bath to remove dust-sized particles by decantation until a clear solution was obtained. The material was then dried overnight at 50 °C and chips of the fractions 0.5-1 mm and 250-500 μm were carefully examined and handpicked under a binocular microscope. The freshest glass and whole-rock fragments (without coatings or vesicle fill) were picked for subsequent chemical analyses. Whole-rock chips were pulverized in a two-step process using an agate mortar grinder and an oscillating disc mill or planetary ball mill, depending on the amount of available material. A subset of 0.5-1.0 mm sized glass and whole-rock chips was used for Sr, Nd and Pb isotope analyses.

3.1 ^{40}Ar/^{39}Ar dating methods

Eleven rock samples from nine seamounts were dated (Table A1 and Fig. A2) using the ^{40}Ar/^{39}Ar laser step-heating technique. Matrix (n=5) and glass (n=9) particles were handpicked from crushed and sieved splits (250-500 μm) and washed and cleaned using an ultrasonic disintegrator.

Separates were irradiated for 6 hours in aluminum trays and capsules in the cadmium shielded RODEO tube of the HFR facilities (NRG, Petten, The Netherlands). The neutron flux was monitored using Taylor Creek Rhyolite Sanidine (TCR-2: 27.87 ± 0.04 Ma; Lanphere and Dalrymple, 2000). $^{40}Ar/^{39}Ar$ laser step-heating analyses were carried out at the GEOMAR Geochronology Lab using a 20 W SpectraPhysics Argon-Ion laser and an MAP 216 series noble gas mass spectrometer. Ar Isotope ratios from mass spectrometry were corrected for mass discrimination, background and blank values, and J-value gradients. Correction factors applied to interfering neutron reactions on Ca and K are ($^{40}Ar/^{39}Ar$) K: 0.00183, ($^{39}Ar/^{37}Ar$) Ca: 0.000699, and ($^{36}Ar/^{37}Ar$) Ca: 0.000270) (Wijbrans et al., 2007).

The step-heating data are evaluated on age spectra diagrams (apparent age and error versus cumulative ^{39}Ar) to detect plateaus (>3 consecutive steps comprising >50 % of the ^{39}Ar released, with ages overlapping within 2 sigma errors). Plateau ages represent the inverse-variance weighted mean of the plateau step ages and errors. The MSDW (mean square weighted deviates; should be <<3) and POF (probability of fit; should be >0.05 at 2 sigma = 95 % confidence levels; Baksi, 1999)are used to evaluate the statistical robustness of plateaus and plateau ages.

3.2 Major-elements

Major-element compositions of fresh glass were obtained using the JEOL JXA-8200 Electron Microprobe (EPMA) at GEOMAR on mounted chips. A single mount (ø = 1 ") contained up to 36 samples with three to four chips from each sample immersed in a two-component epoxy resin-based adhesive. The major-element concentrations were determined with an accelerating voltage of 15 kV and a spot size of 5 μm. Five spots per sample were measured and averaged. Standards used

were VG-A99 (basaltic glass, Makaopuhi Lava Lake, HI) for P_2O_5, FeO, SiO_2, K_2O, CaO, TiO_2, VG-2 (basaltic glass, Juan de Fuca Ridge) for Na_2O, MgO, Al_2O_3, MnO and Scapolite (Meionite, Brazil) for SO_3 and Cl (Jarosewich et al., 1980). The reproducibility for all elements is below 3 % relative standard deviation (RSD), except for P_2O_5 with 6.2 % RSD and MnO 20.2 %RSD and with an accuracy better than 2 %, except 12.2 % for MnO.

Major-elements of whole-rock and glass samples were determined by X-Ray Fluorescence Analyses (XRF) on fused pellets using a Magix Pro PW 2540 XRF at the Institute of Mineralogy and Petrography at the University of Hamburg and for three samples by inductively coupled plasma optical emission spectrometry (ICP-OES) at Acme Analytical Laboratories (Vancouver) Ltd. Loss on ignition (LOI) was determined by mass differences after glowing 1 g of sample in a furnace at 1,050 °C for several hours. For XRF measurements, the following standards were measured along with the samples JGB-1, JB-3, JB-2, JA-3, JG-3 and JG-2. The accuracy for most of the elements lies within 3 % of the reference values suggested by GeoReM (http://georem.mpch-mainz.gwdg.de/).

ICP-OES instrument stability was determined by repeated measurements of STD SO-18 and all elements reproduce better than 1 % RSD except for P_2O_5 with 4.8 % RSD and MnO with 1.4 % RSD. The reproducibility was controlled by duplicate sample digests (SO208 DR53-1, DR55-2) which was below 1 %RSD, except P_2O_5 with 3.8 % RSD. Three procedural blanks were measured to monitor external contributions during sample preparation, which were found to be insignificant (<0.01 for SiO_2, Al_2O_3, MgO, CaO, Na_2O, K_2O, TiO_2, P_2O_5, MnO, <0.04 for Fe_2O_3 and <0.002 for Cr_2O_3). The international reference materials BIR-1 (USGS Reykjanes Peninsula basalt) and BCR-2 (USGS Columbia River basalt) measured along with the samples compare within 5 % of the values recommended by GeoReM. Major-

element data of the analyzed CPS samples are provided in the electronic appendix (Table A1).

3.3 Trace-elements

Trace-element concentrations of glass chips were determined by laser ablation inductively coupled plasma mass spectrometry (LA-ICP-MS) at the Institute of Geoscience, University of Kiel, using a Coherent GeoLasPro Plus 193 nm Excimer laser coupled to an Agilent 7500cs quadrupole ICP-MS. A newly designed large-volume ablation cell (LDHCLAC cell, Trace-element and Microanalysis Group, ETH Zürich) was used in all experiments. Spot size of the laser beam was 80 µm with a repetition rate of 10 Hz and 80 s total acquisition time. The blank signal was measured 20 s prior to each ablation and used for calculation of the actual detection limits. Helium being the carrier gas @ 1.0 l/min was subsequently mixed with Argon @ 0.8 l/min before introduction into the ICP-MS. Calcium (44 m/z) was used for internal standardization. The software Glitter (Macquarie Univ., Australia) was used for data integration of time-resolved signals. Glass SRM NIST612 (preferred values from Jochum et al., 2011; Pearce et al., 1997) was used for instrument calibration, and analytical quality was monitored by repeat analyses of the glass reference material (RM) BCR-2G. Additionally, at the beginning and end of each analytical session (one per day), the MPI-DING glass RMs KL-2G (Kilauea basalt), St.HS. 6/80-G (St. Helens andesite), GOR128-G and GOR132-G (Gorgona komatiites) (Jochum et al., 2006) were analyzed and used for a second step of matrix-matched calibration. Typically, precision as estimated from 40 (DING glasses) to 400 (BCR-2G) repeat analyses was better than 4 %RSD (1σ) for all elements at concentrations significantly above detection limits. Accuracy of results for all analyzed RM can be evaluated from Table A2. Average precision of duplicate sample analyses performed

during different sessions on different days was 5 %rel. (range 1-8 %rel.) except Mo, Cs (12 and 16 %rel.).

Trace-elements of whole-rock samples were analyzed by solution ICP-MS using an AGILENT 7500cs ICP-MS quadrupole instrument at the Institute of Geosciences, University of Kiel. Between 100 and 250 mg sample powder was digested during a multi-step table-top procedure in sealed PFA vials, following the method described in Garbe-Schönberg (1993) with few modifications. Prior to analysis the final solution was diluted 50-fold and spiked to 2.5 µg/l beryllium, indium, rhenium for internal standardization. Analytical accuracy is monitored through international rock standards of BIR-1, BHVO-2 and BCR-2 that were digested and analyzed along with the samples. The measured values for the standards typically lie within 3 % of the values recommended by GeoReM. Precision is better than 1 %rel. for replicates of sample digests and instrumental analysis. Trace-element data for the samples and standards is provided in the electronic appendix Table A2 and Table A3 respectively.

3.4 Isotopic data

Thermal ionization mass spectrometry (TIMS) at GEOMAR was used to determine radiogenic isotope ratios of Sr, Nd and Pb double spike (DS). The isotope analyses were carried out on 100-250 mg of volcanic glass and/or whole-rock chips weighted into 15 ml PFA vials. First, the chips were leached in 2 N HCl at 70 °C for one hour and repeatedly rinsed with 18.2 MΩ/cm H_2O to remove possible signs of alteration and the effects of sample handling. Then the samples were dissolved, in a 5:1 mixture of concentrated ultra-pure HF and HNO_3 at 150 °C for 48 hours, Element separation followed the method described in Hoernle et al. (2008).

Pb isotope ratios were determined on a Finnigan MAT262 RPQ2+, operating in static multi-collection mode. All Pb isotope ratios were mass bias corrected using the

[207]Pb-[204]Pb double spike technique of (Hoernle et al., 2011). The reproducibility of NBS981 (n = 36) is [206]Pb/[204]Pb = 16.9413 ± 0.0024 (2σ), [207]Pb/[204]Pb = 15.4988 ± 0.0025 (2σ), and [208]Pb/[204]Pb = 36.7236 ± 0.0063 (2σ). Replicate analysis (n=6) of samples in terms of separate sample digests are within the external errors of NBS981.

The measurements of Sr and Nd isotopic ratios were performed on a Thermo Scientific TRITON, operating in static multi-collection mode. Sr and Nd isotope ratios were normalized within run to [86]Sr/[88]Sr = 0.1194 and [146]Nd/[144]Nd = 0.7219, respectively. All Sr isotope data are reported relative to NBS987 with [86]Sr/[88]Sr = 0.710250 ± 0.000010 (2σ; n = 63). The Nd isotope data are reported relative to the La Jolla standard with [143]Nd/[144]Nd = 0.511850 ± 0.000007 (2σ; n = 45). Our in-house Nd monitor Spex gave [143]Nd/[144]Nd = 0.511715 ± 0.000006 (2σ; n = 38) for the same period. Samples were replicated within the external errors of NBS987 and La Jolla. Some whole-rock chips, however, yielded high, seawater-altered [87]Sr/[86]Sr. Therefore [87]Sr/[86]Sr was reanalyzed on powders leached with 6 N HCl at 150 °C for 72 hours and then repeatedly rinsed in 18.2 MΩ/cm H2O prior to dissolution. As is evident from Sr-Nd isotope correlations (not shown), this measure resulted in [87]Sr/[86]Sr ratios closer to magmatic values. Replicate analyses of tholeiitic sample SO208 DR1-1 (inverted triangles below the NHRL in Fig. 7a) yielded Nd isotope ratios within error but [206]Pb/[204]Pb could not be reproduced (4 digests of separate handpicked chip populations) within error. Replication of the Nd isotope ratio is consistent with the Sm-Nd isotope system being relatively resistant to seawater alteration due to the fluid immobility of the Rare Earth Elements (REE). The high μ (= [238]U/[204]Pb) ~42 and low Th/U of ~0.30 values of this sample indicate a complex alteration history for this sample with variable U uptake and loss through seawater alteration leading to an under-correction for radiogenic ingrowth.

4. Results

4.1 ^{40}Ar/^{39}Ar age dating

The analyses were carried out on glass (gl, 9 analyses) and/or matrix (mx, 5 analyses) material. The ^{40}Ar/^{39}Ar ages for the Cocos Plate Seamounts range from 7.1 ± 1.0 Ma to 24.0 ± 1.0 Ma, but no clear age progression or correlation with estimated crustal age (Barckhausen et al., 2001) is observed (Table 1). A representative selection of plateau diagrams is shown in Figure 2 (plateau diagrams of all dated samples, including multiple age determinations are shown in appendix Figure A2). Multiple ^{40}Ar/^{39}Ar ages determined on different splits of the same sample set usually reproduced within error (TVG22-3; DR25-2; DR33-1). Samples from three different dredge hauls on Bend Fault Seamount yielded widely differing ages of 24.0 ± 1.0 Ma (DR23-5), 22.5 ± 0.9 Ma (DR24-6) and 10.9 ± 1.8 Ma (DR25-2_wr; weighted mean age) with an age difference of ~12 Ma. A sample from nearby Little Bend Seamount yielded a similar age of 11.3 ± 2.4 Ma (DR26-2_wr) to the younger sample from Bend Fault Seamount.

^{40}Ar/^{39}Ar ages along with the geomagnetic polarity ages of the underlying ocean crust are shown in Table 2. In order to determine if the samples formed on or near the spreading center or in an intraplate setting, we have divided our samples into the following groups:

I) near-ridge CPS samples (DR6-2, DR23-5, DR24-6, DR33-1) with ages within 2 Ma of the estimated paleomagnetic crustal ages and therefore they were erupted <130 km away from the ridge axis, based on a half spreading rate of 65 km/Myrs (Lonsdale, 1988);

II) intraplate CPS samples (DR1-1, DR15-4, DR21-3, TVG22-3, DR25-2, D26-2, DR30-4) with ages more than 2 Ma younger than the estimated paleomagnetic crustal age beneath the volcano and thus they were erupted more than 130 km away from the EPR ridge;

III) undated CPS samples for which no ages were determined.

4.2. Petrography

In general the condition of the sampled glasses and whole-rocks varies from fresh to moderately altered. Signs of alteration include altered olivine, vesicles filled with secondary minerals, such as calcite and zeolites, veins of calcite or zeolite, and thin coatings of Mn. Such material was avoided by handpicking of the samples to obtain the freshest material. Fresh glass rinds were found on some of the samples. Most samples are characterized by a glomeropophyric texture with varying amounts of olivine and plagioclase. Clinopyroxene, spinel and Fe-Ti-oxide (magnetite, ilmenite) phenocrysts are present in some samples.

Samples from near-ridge seamounts contain olivine and plagioclase as the main phenocrysts and clinopyroxene is sometimes present in the groundmass. Samples from intraplate seamounts contain phenocrysts and glomerocrysts of primarily plagioclase, clinopyroxene and Fe-Ti-oxides (ilmenite or magnetite) and in some cases also olivine. Some olivine crystals have spinel inclusions and are associated with glomerocrysts of plagioclase of varying size. Samples from seamounts that were not dated represent a mixture of near-ridge and intraplate seamount groups.

4.3 Major-elements

On the total alkali versus silica (TAS; Fig. 2; Le Maitre et al., 1989) diagram the CPS formed in close proximity to the EPR ridge axis have tholeiitic composition with the exception of one slightly alkaline basalt. Seamounts formed in an intraplate setting range from tholeiitic to alkaline basalt to hawaiite composition (Fig. 3). The MgO contents of the samples vary between 9.3 and 3.1 wt.% and Mg-numbers (Mg# = mol(Mg/(Mg+Fe^{2+}))) from 0.67 to 0.37, indicating the presence of some fairly primitive compositions. Samples generally do not form good correlations on binary diagrams with MgO (Fig. 4a-d). With decreasing MgO, crude increases are observed for Al_2O_3, TiO_2, Na_2O, P_2O_5 and K_2O (e.g. Fig. 4d). The alkaline basalts and hawaiites generally have lower CaO but higher TiO_2, Na_2O and P_2O_5 (e.g. Fig. 4b) than the tholeiitic samples at a given MgO. The lack of good correlations on diagrams with MgO implies that the lavas from the seamounts are not the product of crystal fractionation from a common parental magma, which is also evident from the presence of both tholeiitic and alkalic compositions and the large age range.

Although most mafic (MgO >7 wt.%) CPS lavas overlap with reference EPR-MORB between 10 °N and 10 °S (gray field), the CPS evolve differently from EPR-MORB. In contrast to EPR lavas where SiO_2, FeO^T (FeO + Fe_2O_3), TiO_2 and P_2O_5 increase with decreasing MgO, the tholeiitic samples from the seamounts show no increase in these oxides with increasing differentiation (Fig. 4a, c). The lack of an increase in FeO^T and TiO_2 with decreasing MgO, suggests differentiation of magnetite. CaO contents of the seamount lavas remain either constant or decrease, as in EPR-MORB, with decreasing MgO. Al_2O_3 decreases with decreasing MgO in EPR-MORB, in the CPS lavas it increases to 4 wt.% MgO, indicating clinopyroxene fractionation before significant plagioclase fractionation (Fig. 4b, d).

4.4 Trace-elements

The CPS lavas display a wide range in trace-element composition ranging from highly-depleted incompatible element compositions, slightly more depleted than common D- and N-MORB through E-MORB to more OIB-like compositions (Gale et al., 2013; Fig. 5). The most depleted compositions overlap with depleted compositions a) from the Galápagos Islands, such as found on Genovesa (Fig. 6a; White et al., 1993) and b) EPR-MORB formed during superfast spreading, when the ridge was contaminated with Galápagos plume material that got progressively depleted in incompatible elements due to ongoing melt extraction while flowing beneath the ridge system (Geldmacher et al., 2013; Fig 6a).

Trace-element compositions of near-ridge seamount lavas fall between average N-MORB and OIB (Fig. 5a). Lavas formed in an intraplate setting display greater variations in highly-to-moderately incompatible element composition, with some being more depleted than D-MORB (Fig. 5b). Highly incompatible elements show a large range in concentrations in the intraplate, for example Nb varies from 1.3 ppm in DR1-1 to 57.8 ppm in DR15-4. In the mafic samples with MgO >7 wt.%, the alkaline basalt has the greatest incompatible element enrichment (e.g. highest La/Yb ratios) and also the most heavily fractionated HREE element ratios (with the highest Sm/Yb and Tb/Yb) and TiO_2/Yb, above those commonly observed in MORB (Fig. 6b), indicating the presence of small amounts of residual garnet. Lavas from the undated seamount group show a similar range in highly-to-moderately incompatible element compositions as the dated seamount groups but cover a much wider range (e.g. Nb ranging from 0.53 ppm for DR31-2 to 92.5 ppm for DR30-2). No clear differentiation between the three different age groups can be made, except that intraplate and undated seamount samples show a larger range than observed for near-ridge seamount samples.

More to less incompatible element ratios (e.g. Nb/Yb, La/Yb, La/Sm, Sm/Yb, Tb/Yb, TiO_2/Yb) form positive correlations (e.g. Fig. 6a, b). On a Nb/Yb versus TiO_2/Yb plot (Fig. 6b; Pearce, 2008), all mafic samples (MgO >7 wt.%) plot within or on the boundary of the N-MORB array.

4.5 Isotope Ratios

The measured Sr-Nd-Pb isotope ratios of the CPS lavas are highly variable and range from depleted MORB-like ratios to enriched OIB-like compositions. Initial isotope ratios are shown, assuming $^{40}Ar/^{39}Ar$ ages for dated samples apply to all samples in a dredge and assuming that samples from undated dredges have the same age as the underlying crust (thus representing a maximum age for the samples). Maximum corrections for radiogenic ingrowth of ^{143}Nd, ^{206}Pb and ^{208}Pb are significant and indicated by a double headed arrow in Figure 7.

Overall the lavas form a positive correlation on Pb isotope correlation diagrams (e.g. Fig. 7a) and an inverse correlation on Pb versus Nd isotope diagram (Fig. 7b) with the alkaline samples having the most enriched isotopic compositions and tholeiitic the most depleted. Isotope correlation diagrams of Pb and Nd with Sr (not shown) describe a similar pattern with an inverse correlation on the Sr versus Nd diagram and a positive correlation on the Pb versus Sr plot. Even though the freshest material was picked for isotope analyses the correlation plots with Sr show signs of alteration for some samples with elevated $^{87}Sr/^{86}Sr$ ratios for a given $^{143}Nd/^{144}Nd$ ratio. Seamount SO144-1 (also called "Nicaragua Seamount"; Werner et al., 2003) is located further to the north, off the coast of Nicaragua, and plots at the depleted end of the CPS array. Noteworthy is that EPR Basement formed during superfast spreading trends into the Central Galápagos domain, while the CPS lavas trend into the Northern Galápagos Domain field.

5. Discussion

5.1 Source components contributing to the geochemical composition of the Cocos Plate Seamount lavas

The CPS lavas have many major and trace-element similarities with MORB from the EPR. Basaltic samples fall almost completely within the equatorial EPR field on the TAS diagram (Fig. 3). The most mafic samples (MgO >7 wt.%) almost completely overlap the MORB field in major and minor elements (e.g. Fig. 4). The incompatible trace-element compositions of the CPS lavas completely overlap the N- and E-MORB range from the equatorial EPR, but extend to slightly more depleted incompatible element abundances (Fig. 6a) and more to less incompatible element ratios (Fig. 6b). These differences require either a) variations in conditions of melting from MORB, e.g. higher and lower degrees of melting and/or remelting (previous melt extraction) to derive the more depleted compositions, or b) involvement of more enriched and depleted source material than generally present in the MORB source, e.g. enriched and depleted plume components as occur at the Galápagos hotspot (Harpp and White, 2001; Hoernle et al., 2000; White et al., 1993). Low TiO_2/Yb, Sm/Yb and Tb/Yb (not shown) of the samples point to generation through shallow melting, consistent with upwelling and melting beneath young (<25 Ma) crust and thus thin lithosphere, even for the intraplate seamounts.

The isotope data for the seamount lavas require the involvement of an enriched OIB type component. The positive correlations formed on the Pb vs Pb and Sr isotope diagrams and negative correlation on Sr and Pb versus Nd isotope diagrams can be explained by mixing of a Northern Galápagos Domain component (located on the northern side of the plume; Geldmacher et al., 2003; Hoernle et al., 2000; Werner et al., 2003) with either the equatorial EPR-MORB source or a depleted Galápagos

plume component, such as observed in Genovesa lavas (Fig. 7). Specifically, two component mixing between the most enriched northern Galápagos endmember as represented by sample SO81-10/17 from the Seamount Province offshore Costa Rica (Hoernle et al., 2000) and a depleted MORB-like endmember represented by sample SO144 2 DR-1 from the fossil GSC between the Carnegie and Malpelo Ridges (Harpp et al., 2005; Werner et al., 2003) in a 30:70 proportion (solid black mixing line with increments of 10 % in Fig. 7) can explain the isotope data.

Correlations of isotope with incompatible element ratios, however, indicate that at least two depleted components must be present with similar (but not identical, for example in Nd) isotopic compositions. Correlations of Pb and Nd isotope ratios with incompatible element ratios (e.g. Tb/Yb, La/Nd and Ce/Pb) of the seamount lavas (Fig. 8) are not consistent with two component mixing. In particular, plots with ratios with the same denominator (e.g. $^{143}Nd/^{144}Nd$ vs La/Nd and $^{206}Pb/^{204}Pb$ vs Ce/Pb) should produce well-defined linear correlations if only two components are involved. Therefore, at least two depleted components are required to explain the variability in samples with low Tb/Yb, La/Nd and Ce/Pb. One of these components could be EPR-MORB, but the second component with lower Tb/Yb, La/Nd and Ce/Pb could either be depleted plume material or EPR-MORB that has undergone more than one stage of melting (melt extraction event). The later process was proposed by Geldmacher et al. (2013), to explain the lower concentrations of incompatible element ratios in Galápagos plume material reaching the EPR during superfast spreading in the Miocene.

5.2 Formation of near-ridge seamounts

The three Cocos Plate Seamounts with similar ages to the underlying crust (22.4-24 Ma) have similar trace-element and nearly similar or just slightly more

enriched isotopic compositions to EPR-MORB of similar age, e.g. ocean crust drilled

at Deep Sea Drilling Project (DSDP) Site 495. This ocean crust formed at the EPR at

~5 °N just at the beginning of EPR super fast spreading and the onset of Galápagos

plume material reaching the EPR (Fig. 9). The newly formed GSC is likely to have

opened a pathway for mantle material to flow westward from the Galápagos plume

into the EPR (Geldmacher et al., 2013), which was enhanced by the onset of

superfast spreading. As shown by Niu and Hékinian (2004), the flow of plume

material to a spreading ridge ("ridge suction") increases with spreading rate. During

the peak of superfast spreading (between 18 and 11 Ma ago), the composition of

equatorial EPR-MORB formed between 3 °S and 7 °N shows clear evidence for the

influx of isotopically enriched Galápagos plume material displaying a peak

$^{206}Pb/^{204}Pb$ isotope ratio at ~17 Ma. The third near-ridge seamount sample (open

diamond in Fig. 9) erupted at around 16.5 Ma ago shortly after the geochemical peak

in EPR generated crust and yields the most radiogenic Pb isotope ratios of all near-

ridge seamount samples in accordance with the proposed model of Geldmacher et

al. (2013; thick black temporal isotopic evolution curve in Fig. 9). Therefore, we

propose that the near-ridge seamount samples represent seamounts that formed in

close proximity to the EPR with varying isotopic composition depending on the flux of

plume material spreading along the EPR axis.

5.3 Formation of intraplate Cocos Plate Seamounts

5.3.1 Transport of plume material beneath the Cocos Plate

The major-element geochemistry of the intraplate seamount group is consistent

with an intraplate origin. On the MgO versus Al_2O_3 diagram, the more evolved (lower

MgO) samples deviate completely from the MORB differentiation array. The increase

in Al_2O_3 and decrease in CaO with decreasing MgO for the younger (and some

undated) samples indicates that olivine and clinopyroxene are the main fractionating phases in these samples between MgO of 8 to 4 wt.%. Olivine and clinopyroxene on the liquidus instead of olivine and plagioclase points to high-pressure crystal fractionation (>0.5 GPa or ~15-17 km depth), resulting from the shrinkage of the plagioclase in favor of the clinopyroxene stability field with increasing pressure (e.g. Bernstein, 1994; Thompson, 1974; Yoder and Tilley, 1962). Deeper depth of differentiation than for EPR lavas is consistent with these seamounts having on thicker crust, i.e. well off-axis or in an intraplate setting, compatible with the younger ages obtained on some of these samples.

Approximately half of the intraplate samples have more enriched (radiogenic) Pb isotope compositions than EPR-MORB (Fig. 7), but it is unlikely that enriched plume material flowing beneath the GSC to the EPR was then transported along the deepening base of the lithosphere away from the EPR ridge axis. Plate tectonic reconstructions showing the paleo-positions where the younger seamounts formed (after Meschede and Barckhausen, 2001) are displayed in figures 10a-f. In accordance with Werner et al. (2003), the position of the GSC relative to the Galápagos hotspot changed several times due to multiple ridge jumps, abandoning old (dashed thick black lines in Fig. 10) and establishing new (solid thick black lines in Fig. 10) ridge systems. These ridge jumps resulted in varying configurations between the plume and the GSC. Assuming a fixed position of the Galápagos hotspot and an average Cocos Plate motion velocity of 78 mm/a to the NE for the past 24 Ma (personal communication with U. Barckhausen), the seamounts formed between 400 and 900 km away from the hotspot, when it was located either north or directly beneath the GSC.

On the isotope correlation diagrams, the seamount samples form linear arrays that can be explained through mixing of up to 30 % Northern Galápagos plume

component with shallow depleted, presumably upper asthenosphere and/or lithospheric mantle. Therefore mantle from the northern domain of the Galápagos plume appears to have spread out at least 400-900 km northwards beneath the Cocos Plate. In contrast, Central and/or Southern Domain Galápagos plume material appears to have flowed along the GSC into the EPR during superfast spreading (see Fig. 7 and Geldmacher et al., 2013). These observations are consistent with plume-ridge interaction of a zoned mantle plume with the northern portion (Northern Domain) of the Galápagos plume being primarily located north of the GSC and the central and southern portions (Central and Southern Domains) primarily beneath or south of the GSC during the formation of the CPS from 23 to 7 Ma. Cessation of seamount formation after 7.1 Ma (the age of the youngest seamount; Fig. 10e) coincides with the GSC moving to the north of the plume (Sallarès et al., 2003; Werner et al., 2003; Wilson and Hey, 1995). The location of the spreading center north of the hotspot no doubt inhibited plume material from flowing beneath the Cocos Plate as it did during the Early to Middle Miocene when the GSC was more or less above the plume.

5.3.2 Model for the Origin of the Intraplate Cocos Seamounts

In this section, we propose two endmember type models to explain the origin of the Cocos Plate Seamounts (Fig. 11). An important factor in the origin of these intraplate volcanic structures is that they formed on EPR generated crust/lithosphere. Bearing in mind the geochemical composition of the CPS lavas, the formation of the Cocos Plate Seamounts requires northward lateral transport of Galápagos plume material.

The first model is based on differences in crustal and/or lithospheric thickness between EPR and GSC generated crust/lithosphere. The crust formed at the GSC

near the Galápagos hotspot is >8 km thick (Detrick et al., 2002), whereas crust generated further away from the hotspot at the EPR at present is thinner (4-6.5 km between 9-10 °N; Aghaei et al., 2014; Klein, 2003). Investigations of the seismic structure of the hotspot tracks yielded crustal thicknesses varying from ~17-21 km for the Cocos Ridge and ~13-19 km for the Carnegie Ridge (Sallarès et al., 2005; Walther, 2003). The differences in crustal thickness alone lead to differences in possible lithospheric thickness of up to 14 km going away from the hotspot.

Since the geochemistry indicates that shallow melting of enriched Galápagos plume material is involved in the origin of these seamounts (Fig. 6), we propose that plume material from the Northern zone of the Galápagos plume flowed northwards along the base of the lithosphere. As the plume material flows, it incorporates depleted asthenosphere (Phipps Morgan and Morgan, 1999). As this stirred together mantle flows from the base of the thicker GSC lithosphere to thinner EPR lithosphere, it ascends and melts by decompression (Fig. 11a). Even though the seamounts formed on EPR crust formed during super-fast spreading when Galápagos material contributed to crustal formation, there is likely to have been an inverted step in lithospheric thickness between crust formed along the two different spreading centers or at the RSB. Once plume material reached the EPR, it would have been diverted both north and south along the ridge, thus at the triple junction there would have been an abrupt decrease in the amount of plume material flowing in either direction along the EPR. Such an inverted step in the base of the lithosphere would have facilitated upwelling to the north of the RSB, causing enhanced decompression melting.

The formation of seamounts and their exact locations are likely to reflect preferential ascension of plume material, including entrained asthenosphere, at the shallowest parts (e.g. inverted troughs) in the base of the lithosphere, where melts

can pool and then ascend to the surface (e.g. Demidjuk et al., 2007). Lithospheric

weaknesses, e.g. tectonic structures such as fracture zones, are also likely to have

served as pathways to channelize magmas ascending to the surface. Such pathways

can also be used by later melts, as is evidenced at Bend Fault seamount where at

least two episodes of volcanism more than 10 Ma apart are recorded.

The second model to explain the far-field lateral transport and melting of

Galápagos plume material is the deflection of ascending plume material at the base

of a restitic viscous plug at the base of the lithosphere (Fig. 11b; Hall and Kincaid,

2003). Higher seismic velocity observed beneath hotspots is likely to reflect the

presence of higher viscosity plume residue, resulting from dehydration through melt

extraction from the central region of an upwelling plume (Phipps Morgan et al., 1995).

Upwelling plume material that encounters such a high viscosity lid cannot ascend any

further and is therefore deflected horizontally until it reaches the margins of the

restitic plug. At the edge of the viscous lid, the fertile plume mantle can ascend

further resulting in melting beneath the overlying Cocos Plate, generating intraplate

volcanism, far away from the ridge and plume center (Hall and Kincaid, 2003).

Ponding of restitic plume material beneath the thin lithosphere at and near the

spreading center could allow some of the upwelling plume material to be deflected

northwards away from the plume and the ridge. Of course, some fertile plume

material still manages to upwell beneath the ridge to generate new crust at the ridge,

facilitated by extension and separation of the restitic plug directly beneath the ridge.

The aforementioned models are not mutually exclusive and could both contribute to

the formation of intraplate volcanism beyond the morphological hotspot track(s)

formed by the plume.

Based on satellite altimetry (Smith and Sandwell, 1997), the Cocos Plate

Seamount province may be twice the size of the study area, extending to the SW

parallel to the RSB onto crust that is ~6-8 Ma in age. The absence of the seamount province on the younger crust most likely reflects the GSC passing northwards over the hotspot, cutting off the flow of plume magma to the north.

5.3.3 Comparison with the Arch Volcanic Fields near Hawaii

Here we compare the Cocos Plate Seamounts with the North and South Arch Volcanism related to the Hawaiian hotspot, but not a part of the morphological Hawaiian hotspot track, to evaluate if they may have formed by similar mechanisms. The Hawaiian-Emperor seamount chain is the most pronounced bathymetric anomaly related to a hotspot track that is characterized by a narrow (100-200 km), 5,800 km long volcanic tail extending from the active Hawaiian Volcanoes to Kamchatka (Duncan and Keller, 2004). The width of the hotspot track and seismic tomographic images (e.g. Montelli et al., 2006; Montelli et al., 2004) suggest that it is being fed by a mantle plume (conduit) of similar diameter to the width of the hotspot track. Nevertheless, large outpourings of silica-undersaturated volcanic rocks (alkali basalts, basanites and nephelinites) have been found to the north of the islands near the Molokaii Fracture Zone (North Arch Volcanic Field) and southeast of the Big Island (South Arch Volcanic Field) and are thought to be related to the Hawaiian hotspot as discussed below (white areas in Fig.12b).

The North Arch Field is located 200-400 km north of Oahu and covers an area of 25,000 km^2 erupted within the last c. 2 Ma. Although ~100 volcanic edifices, ranging from steep-sided cones to ridge-like structures to low shields, have been identified, most of this volcanic province is covered by sheet flows, less than 10 m thick in most places, resulting in an estimated volume of 1,000-1,250 km^3 for the North Arch Field (Clague et al., 2002; Frey et al., 2000) and have been referred to as "alkalic flood basalts" (Clague et al., 1990). The extensive lava fields of the Hawaiian

North Arch are related to fissure eruptions along pre-existing zones of crustal weakness, such as the 75 km long NNW trending faults related to the Molokaii Fracture Zone (Clague et al., 2002). The South Arch volcanic field, located 175-200 km south of the Big Island of Hawaii, comprises several young lava fields, formed within the last c. 10 ka, with the largest one covering an area of 35 by 50 km (Lipman et al., 1989). The major and trace-element and Sr, Nd and Pb isotopic compositions of the Arch lavas are similar to the rejunvenated stage volcanism on the Hawaiian Island volcanoes, which generally occurs several million years after the main volcanic shield has formed when the volcano is no longer located over the hotspot. Therefore it is likely that the rejuvenated stage and Arch lavas were formed by similar processes and have a common origin (e.g. Frey et al., 2000; Yang et al., 2003).

The CPS and Arch lavas show a number of distinct but also some similar features and geochemical characteristics. Despite the weaker buoyancy flux of the Galápagos plume, the CPS were formed at greater distances from the hotspot (400-900 km) than the Arch lavas (within 400 km of the Hawaiian Islands). The Cocos Plate Seamounts, however, form larger volcanic structures (up to 2,000 m high and 14 km along the longest axis) than the Arch lavas (<700 m high and <7 km long), but cover a much smaller area (≥2,100 km^2) and the volume of the seamount structures (~620 km3, estimated from bathymetric mapping data after Yeo et al., 2013) are much lower. There is no evidence for extensive extrusions of sheet flows over large areas of the seafloor associated with the CPS, but even if such massive outpourings of sheet flows occurred, they have, no doubt, been covered by sediments. Therefore it is not possibly to compare volumes of CPS-province volcanism with that of the Arch lavas.

The Arch lavas have distinct major and trace-element compositions from the Cocos Plate Seamounts. The silica-undersaturated nature (Fig. 2) and the high 1)

concentrations of incompatible elements, 2) more to less incompatible element ratios (e.g. La/Yb, La/Sm, Nb/Yb) and 3) middle to heavy rare earth element ratios (e.g. Sm/Yb, Tb/Yb) and TiO_2/Yb ratios (Fig. 5), despite depleted isotopic compositions of the Arch and Rejuvenated lavas point to generation by low degrees of partial melting of peridotite within the garnet stability field (e.g. Clague and Frey, 1982; Frey et al., 2000). In contrast to the Arch lavas, the Cocos Plate Seamount province consists of primarily tholeiite with lesser volumes of alkaline basalt and hawaiite, which formed through melting of spinel peridotite at shallow depths with minor amounts of garnet only in the residuum of the alkalic magmas (Fig. 6). In summary, the difference in major and trace-element compositions can be explained through high degrees of melting beneath young (<25 Ma), thin (~40-50 km) lithosphere to produce the Cocos Plate Seamounts and low degrees of melting beneath old (~90 Ma), thick (90-100 km) lithosphere the silica-undersaturated Arch and rejuvenated lavas.

Although the isotopic compositions of the Arch lavas and CPS are distinct, they both point to mixing of plume material with depleted upper asthenosphere and/or lithosphere. The Sr-Nd-Pb isotopic compositions of the Arch and rejuvenated lavas are intermediate between the Hawaiian plume and Pacific MORB fields (Frey et al., 2000). The high ^{3}He/^{4}He of up to 20 Ra in the South Arch lavas clearly indicates the presence of a plume component (Frey et al., 2000). The source is thought to be a mixture of a Hawaiian plume component with a depleted mid-ocean ridge basalt component (Yang et al., 2003), similar to the CPS. As discussed above, the isotope geochemistry of the CPS can be explained by mixing of an enriched plume-derived component with a depleted component similar to MORB and to a remelted depleted component either from the upper mantle or the plume. Therefore in both areas the volcanism is ultimately related to the interaction of plume material with the upper mantle as the plume material spreads out in the uppermost asthenosphere.

The occurrence of widespread secondary volcanism at Hawaii has been attributed to different mechanisms including a second melting zone in the plume material spreading laterally along the base of the lithosphere (Ribe and Christensen, 1999), decompression melting during lithospheric flexural uplift that surrounds the growing shield volcanoes (Bianco et al., 2005) or interaction of the laterally spreading plume material with the irregular (washboard type) base of the lithosphere generated by small scale convection (Ballmer et al., 2011). For the Hawaiian North Arch volcanism, Yamamoto and Morgan (2009) proposed that off-chain volcanism is related to an offset in lithospheric thickness at the Molokaii Fracture Zone. North of the Molokaii Fracture Zone, the lithosphere is younger and therefore thinner, resulting in increased melting and greater swell height (Phipps Morgan et al., 1995). A similar situation applies to the CPS that formed just north of the transition from thicker, plume-ridge-interaction-influenced GSC lithosphere to thinner, normal mid-ocean-ridge-type lithosphere formed at the EPR.

6. Conclusions

^{40}Ar/^{39}Ar age dating show that the Cocos Plate Seamounts range in age from 22.5 to 7.1 Ma and that some have similar ages to the underlying crust (± 2 Ma) and thus formed near-ridge and others, more than 2 Ma younger than the underlying crust, formed in an intraplate setting. Seamounts that formed in close proximity to the ridge provide further support for the Geldmacher et al. (2013) model, that due to increased ridge suction during super-fast spreading at the EPR, Galápagos plume material flowed beneath the newly formed GSC into the EPR. In contrast, intraplate seamounts can be explained by large-scale distribution of plume material along the base of the lithosphere during times when the hotspot was located north or directly below the GSC. We propose that flow of Northern Galápagos plume material

northwards from the base of the thicker GSC generated crust to thinner EPR crust or along the base of a viscous restitic root upwelling at its edges (or both) resulted in decompression melting that formed the seamounts. In general, the seamount lavas represent a mixture of variable proportions of the enriched Northern Galápagos plume component with a depleted component most likely MORB-like asthenosphere and/or lithosphere but possibly also residual plume material. In comparison to Hawaiian Arch volcanism, represented by voluminous eruptions of highly silica-undersaturated melts, the formation of the Cocos Plate Seamounts, consisting of silica-saturated and slightly undersaturated melts, no doubt reflects spreading out and melting to higher degrees and shallower depths beneath younger and thus thinner lithosphere. The presumably greater volume of the Arch volcanism at Hawaii is likely to reflect the higher buoyancy flux of the Hawaiian plume compared to the Galápagos plume.

territorial waters. This study was funded by the German Federal Ministry of Education and Research (BMBF; Grant 03G0208A SO 208-PLUMEFLUX).

Figure and table captions

Fig. 1: a) Bathymetric overview map of the equatorial East Pacific area showing the major bathymetric features (data are from The GEBCO_08 Grid, version 20091120, http://www.gebco.net; GSC – Galápagos Spreading Center; EPR – East Pacific Rise; CR – Coiba Ridge; MR – Mapelo Ridge; Car. Ridge – Carnegie Ridge, FR – Fisher Ridge, RSB – rough smooth boundary). The rectangle encloses the study area with b) showing a blow up of the study area. Crustal ages inferred from paleomagnetic data are displayed along stippled lines (Barckhausen et al., 2001). Diamonds mark seamounts with $^{40}Ar/^{39}Ar$ ages <2 Ma younger than the underlying crust, inverted triangles mark seamounts >2 Ma younger than the ocean crust, circles mark geochemically studied geochemically studied seamounts, which were not dated. Plate motion vectors are from Wilson (1996) and Barckhausen et al. (2001).

Fig. 2: Representative selection of plateau diagrams, the full set is available in the online appendix. Plateau diagrams a-d for seamounts formed near the EPR ridge axis and e-h for seamounts formed in an intraplate setting.

Fig 3: Silica versus total alkali-diagram (Le Maitre et al., 1989) of the seamount samples, field for EPR-MORB between 10 °N and 10 °S (gray field; PetDB http://www.earthchem.org/petdb), field for Hawaii Arch Field (open field with dashed outline; GEOROCK (http://georoc.mpch-mainz.gwdg.de/georoc/Entry.html) and Rejuvenated lavas (open field with solid outline, Clague and Frey (1982)) and Nicaragua Smnt sampled during R/V Sonne cruise SO144 (star; Werner et al., 2003). Subdivision of volcanic rocks into alkaline and tholeiitic is after MacDonald and Katsura (1964). According to their major-element composition, the Cocos Plate Seamount samples can be subdivided into Hawaiite (HW, black symbols), Alkali Basalts (AB, open symbols) and Tholeiites (TH, dark gray symbols). Symbols with a

cross (+) denote that whole-rock material was analyzed, all other analyses were made on fresh handpicked glass.

Fig. 4: Major-element compositions of the Cocos Plate Seamounts compared with EPR-MORB between 10 °N and 10 °S. Major-element data have been normalized to 100 % on a volatile-free basis. Symbols with a cross (+) markanalyses from whole-rock samples. In general the mafic samples (MgO ≥7 wt.%) overlap with the EPR-MORB field whereas samples with MgO <7 wt.% tend to higher Al_2O_3 and lower SiO_2, FeO^T. In a) Cocos Plate Seamount samples overlap the low SiO_2 end of the EPR array in samples with MgO >5 wt. In b) no clear fractionation trend is observed indicating that the seamounts are not derived from the same parental magma. In c) FeO^T (total iron as FeO) shows almost no correlation with decreasing MgO. In d) Al_2O_3 increases with decreasing MgO in contrast to the EPR-trend, indicating that cpx is a more important fractionating phase in the CPS than in the EPR lavas.

Fig. 5: Multi element diagram for Cocos Plate Seamount lavas compared to average D-, N- & E-MORB (Gale et al., 2013) and OIB patterns (Sun and McDonough, 1989). Incompatible element concentrations have been normalized to primitive mantle (Hofmann, 1988). a) Incompatible element patterns of near-ridge seamount group samples have compositions similar to N- to E-MORB except one sample with OIB-like pattern. b) Incompatible element patterns of intraplate seamount group range from below D-MORB to OIB. Undated seamounts are shown by grey field and cover a similar range in composition as the intraplate seamount group.

Fig. 6: a) $(La/Yb)_n$ versus $(Sm/Yb)_n$ (n indicates normalization to Primitive Mantle after Hofmann, 1988) for samples with MgO >7 wt.%, shows that the Cocos Plate Seamount lavas have similar or slightly more depleted compositions than reference EPR-MORB from 10 °S-10 °N (PetDB) but overlaplargely with Cocos Plate ocean crust formed during superfast spreading at the EPR (Geldmacher et al., 2013). b)

Nb/Yb versus TiO_2/Yb after (Pearce, 2008) for samples with MgO >7 wt.% indicates that melting occurred at shallower depths within the spinel stability field, similar to those at which MORB is generated, consistent with the MORB-like $(Sm/Yb)_n$ ratios. Hawaiian Arch and rejuvenated lavas have more alkaline compositions and most likely formed by lower degrees of melting (higher La/Yb) at greater depths within the garnet stability field (≥70-80 km; Green and Ringwood, 1967; Ringwood, 1967; Robinson and Wood, 1998). Symbols with a cross (+) indicate analyses of whole-rock samples. Symbols with no cross are analyses of glass. Hawaii rejuvenated lavas (open field with solid outline) from Clague and Frey (1982) and (Garcia et al., 2010).

Fig. 7: Initial ^{206}Pb/^{204}Pb versus ^{208}Pb/^{204}Pb and ^{143}Nd/^{144}Nd isotope ratios of CPS form positive and negative correlations respectively, which extend from depleted EPR-MORB-like and/or depleted Galápagos (e.g. Genovesa) components to the enriched Northern Galápagos domain plume composition (Harpp and White, 2001; Hoernle et al., 2000; Werner et al., 2003; White et al., 1993). Thin black line marks NHRL after Hart (1984). The thick black line is a calculated mixing line between SO81 10/17 (Hoernle et al., 2000), the most enriched endmember from the Northern Galápagos domain, and sample 2 DR-1 (SO144; Harpp et al., 2005; Werner et al., 2003), depleted MORB-like endmember from the Cocos Plate crust. Black circles on the thick black line represent increments of 10 % mixing proportions of the Northern Galápagos Component. For comparison, Cocos Plate crust formed during superfast spreading at the EPR (Geldmacher et al., 2013) represents a mixture between a depleted MORB-like component and the enriched Central Galápagos domain suggesting that the Central component is flowing beneath the GSC to the EPR, whereas the Northern component is flowing northwards along the base of the Cocos Plate lithosphere. Symbols with a cross (+) denote that whole-rock material was analyzed. Symbols without a cross denote analyses of glass. Arrow labeled

"Alteration" indicates that two replicates (separately prepared and analyzed chips) of sample SO208 DR1-1 have been affected by seawater alteration (see text for more details). Analytical errors are significantly smaller than symbol size.

Fig. 8: Nd and Pb isotope ratios versus incompatible trace element ratios (($Tb/Yb)_n$, La/Nd, Ce/Pb). To explain the non linear correlations of the samples, especially on plots where the ratios on both axis have the same denominator (b and c), three sources are required: 1) enriched Northern Galápagos domain, 2) depleted EPR-MORB between 10 °N and 10 °S, and 3) remelted residual EPR-MORB and/or depleted Eastern Galápagos Domain material. Galápagos Domains from Harpp and White (2001); Hoernle et al. (2000); Werner et al. (2003); White et al. (1993), EPR-MORB between 10 °N and10 °S is from PetDB, EPR during superfast spreading is from Geldmacher et al. (2013).

Fig. 9: $^{206}Pb/^{204}Pb$ versus age (after Geldmacher et al., 2013). The near-ridge seamounts (diamonds) plot along the geochemical trend (thick black line) for Cocos Plate crust formed at the EPR, during super fast spreading. The three samples from the two oldest seamounts overlap with EPR crust that was generated at the onset of Galápagos plume material spreading beneath the EPR. The third seamount formed shortly after the peak input of Galápagos plume material into the EPR. Shown are also the errors for the older samples (gray squares). For the alkali sample (open square) the error is within symbol size.

Fig. 10: Reconstruction of paleo-positions of near-ridge and intraplate seamounts (paleo-tectonic reconstruction after Meschede & Barckhausen, 2001). Open symbols mark the approximate position where seamounts formed based on an average plate velocity of 78 mm/year. The black star marks the estimated position of the Galápagos hotspot, The seamounts formed between 400 and 900 km away from the current

Galápagos hotspot position during times when the GSC was above or to the south of the Galápagos hotspot (Werner et al., 2003).

Fig. 11: Two endmember models for formation of the Cocos Plate Seamounts. a) Enriched Northern Galápagos domain (blue part of the conduit) material spreads away from the plume stem and flows northwards along the base of the Cocos Plate lithosphere. As the plume mantle flows and ascends along the thinning lithosphere to the north, it undergoes decompression melting causing the formation of the Cocos Plate Seamounts. A likely inverted step in the base of the lithosphere at the Rough Smooth-Boundary (RSB), denoting the boundary between crust formed at the GSC and EPR, could enhance upwelling beneath the southernmost EPR generated lithosphere. b) Dehydration of upwelling plume material through melt extraction could lead to the formation of a viscous restitic root (Hall & Kincaid, 2003) above the plume and beneath the GSC, which would serve to deflect fertile plume material at depth away from the center of the upwelling plume. Northward flow of plume material along the thinning restite would allow plume mantle to continue to ascend and melt by decompression. In accordance with both possible models, seamounts would preferentially form at places where melt pools and/or where there are weaknesses in the lithosphere.

Fig. 12: Comparative map of a) Galápagos and b) Hawaii to visualize the differences in the distance and nature of the far-field transport of plume material. In a) far-field lateral transport of Galápagos plume material leads to the formation of individual volcanic edifices between 400-900 km away from the presumed plume center (CPS; white symbols). Note that due to spreading along the GSC and plate motion, the present location of the Miocene CPS is further from the Galápagos hotspot (relative position reflected by closest part of the hotspot track) then when they formed. In b) the North and South Arch volcanic fields (white areas) formed closer to the Hawaiian

plume center (175-400 km) and represent rather large outpourings of lava on the seafloor. Outlines for the Arch Fields after Bianco et al. (2005).

Table 1: $^{40}Ar/^{39}Ar$ step-heating results. Selected age spectra shown in Fig. 2 are marked with *; weighted mean ages in light gray

Table 2: Seamount name, sample number, rock type, sample location, crustal age beneath seamount (Barckhausen et al., 2001) and $^{40}Ar/^{39}Ar$ plateau age ± 2Sigma error for seamounts (ages marked with * represent weighted mean ages). The samples are divided into near-ridge, intraplate and undated groups. Note that samples from "Bend Fault" seamount display large age variations ranging from near-ridge to intraplate settings.

References

Aghaei, O. et al., 2014. Crustal thickness and Moho character of the fast-spreading East Pacific Rise from 9°42′N to 9°57′N from poststack-migrated 3-D MCS data. Geochemistry, Geophysics, Geosystems, 15(3): 634-657.

Baksi, A.K., 1999. Reevaluation of Plate Motion Models Based on Hotspot Tracks in the Atlantic and Indian Oceans. The Journal of Geology, 107(1): 13-26.

Ballmer, M.D., Ito, G., van Hunen, J., Tackley, P.J., 2011. Spatial and temporal variability in Hawaiian hotspot volcanism induced by small-scale convection. Nature Geoscience, 4(7): 457-460.

Barckhausen, U., Ranero, C.R., von Huene, R., Cande, S.C., Roeser, H.A., 2001. Revised tectonic boundaries in the Cocos Plate off Costa Rica: Implications for the segmentation of the convergent margin and for plate tectonic models. Journal of Geophysical Research, 106(B9): 19207-19220.

Bernstein, S., 1994. High-pressure fractionation in rift-related basaltic magmatism: Faeroe plateau basalts. Geology, 22(9): 815-818.

Bianco, T.A., Ito, G., Becker, J.M., Garcia, M.O., 2005. Secondary Hawaiian volcanism formed by flexural arch decompression. Geochemistry, Geophysics, Geosystems, 6(8): Q08009.

Bowles, J.A. et al., 2014. Eruptive timing and 200 year episodicity at 92°W on the hot spot-influenced Galápagos Spreading Center derived from geomagnetic paleointensity. Geochemistry, Geophysics, Geosystems, 15(6): 2211-2224.

Christie, D.M., Werner, R., Hauff, F., Hoernle, K., Hanan, B.B., 2005. Morphological and geochemical variations along the eastern Galápagos Spreading Center. Geochemistry, Geophysics, Geosystems, 6(1): Q01006.

Clague, D.A., Frey, F.A., 1982. Petrology and Trace Element Geochemistry of the Honolulu Volcanics, Oahu: Implications for the Oceanic Mantle below Hawaii. Journal of Petrology, 23(3): 447-504.

Clague, D.A., Holcomb, R.T., Sinton, J.M., Detrick, R.S., Torresan, M.E., 1990. Pliocene and Pleistocene alkalic flood basalts on the seafloor north of the Hawaiian islands. Earth and Planetary Science Letters, 98(2): 175-191.

Clague, D.A., Uto, K., Satake, K., Davis, A.S., 2002. Eruption Style and Flow Emplacement in the Submarine North Arch Volcanic Field, Hawaii. In: Takahashi, E., Lipman, P.W., Garcia, M.O., Naka, J., Aramaki, S. (Eds.), Hawaiian Volcanoes: Deep Underwater Perspectives. American Geophysical Union, pp. 65-84.

DeMets, C., Gordon, R.G., Argus, D.F., Stein, S., 1990. Current plate motions. Geophysical Journal International, 101(2): 425-478.

Demidjuk, Z. et al., 2007. U-series isotope and geodynamic constraints on mantle melting processes beneath the Newer Volcanic Province in South Australia. Earth and Planetary Science Letters, 261(3-4): 517-533.

Detrick, R.S. et al., 2002. Correlated geophysical, geochemical, and volcanological manifestations of plume-ridge interaction along the Galápagos Spreading Center. Geochemistry, Geophysics, Geosystems, 3(10): 8501.

Duncan, R.A., Hargraves, R.B., 1984. Plate tectonic evolution of the Caribbean region in the mantle reference frame. Geological Society of America Memoirs, 162: 81-94.

Duncan, R.A., Keller, R.A., 2004. Radiometric ages for basement rocks from the Emperor Seamounts, ODP Leg 197. Geochemistry, Geophysics, Geosystems, 5(8): Q08L03.

Farnetani, C.G., Hofmann, A.W., 2009. Dynamics and internal structure of a lower mantle plume conduit. Earth and Planetary Science Letters, 282(1-4): 314-322.

Fisher, A.T. et al., 2003. Abrupt thermal transition reveals hydrothermal boundary and role of seamounts within the Cocos Plate. Geophysical Research Letters, 30(11): 1550.

Frey, F.A., Clague, D., Mahoney, J.J., Sinton, J.M., 2000. Volcanism at the Edge of the Hawaiian Plume: Petrogenesis of Submarine Alkalic Lavas from the North Arch Volcanic Field. Journal of Petrology, 41(5): 667-691.

Gale, A., Dalton, C.A., Langmuir, C.H., Su, Y., Schilling, J.-G., 2013. The mean composition of ocean ridge basalts. Geochemistry, Geophysics, Geosystems, 14(3): 489-518.

Garbe-Schönberg, C.-D., 1993. Simultaneous determination of thirty-seven trace elements in twenty-eight international rock standards by ICP-MS. Geostandards Newsletter, 17(1): 81-97.

Garcia, M.O. et al., 2010. Petrology, Geochemistry and Geochronology of Kaua'i Lavas over 4.5 Myr: Implications for the Origin of Rejuvenated Volcanism and the Evolution of the Hawaiian Plume. Journal of Petrology, 51(7): 1507-1540.

Geist, D.J., White, W.M., McBirney, A.R., 1988. Plume-asthenosphere mixing beneath the Galápagos archipelago. Nature, 333(6174): 657-660.

Geldmacher, J. et al., 2003. Hafnium isotopic variations in volcanic rocks from the Caribbean Large Igneous Province and Gal·pagos hot spot tracks. Geochemistry, Geophysics, Geosystems, 4(7): 1062.

Geldmacher, J. et al., 2013. Influence of the Galápagos hotspot on the East Pacific Rise during Miocene superfast spreading. Geology, 41(2): 183-186.

Graham, D.W., Christie, D.M., Harpp, K.S., Lupton, J.E., 1993. Mantle Plume Helium in Submarine Basalts from the Galápagos Platform. Science, 262(5142): 2023-2026.

Green, D.H., Ringwood, A.E., 1967. The stability fields of aluminous pyroxene peridotite and garnet peridotite and their relevance in upper mantle structure. Earth and Planetary Science Letters, 3(0): 151-160.

Hall, P.S., Kincaid, C., 2003. Melting, dehydration, and the dynamics of off-axis plume-ridge interaction. Geochemistry, Geophysics, Geosystems, 4(9): 8510.

Harpp, K.S., Wanless, V.D., Otto, R.H., Hoernle, K., Werner, R., 2005. The Cocos and Carnegie Aseismic Ridges: A Trace Element Record of Long-term Plume-Spreading Center Interaction. Journal of Petrology, 46(1): 109-133.

Harpp, K.S., White, W.M., 2001. Tracing a mantle plume: Isotopic and trace element variations of Galápagos seamounts. Geochemistry, Geophysics, Geosystems, 2(6): 1042.

Hart, S.R., 1984. A large-scale isotope anomaly in the Southern Hemisphere mantle. Nature, 309(5971): 753-757.

Hey, R., 1977. Tectonic evolution of the Cocos-Nazca spreading center. Geological Society of America Bulletin, 88(10): 1404-1420.

Hoernle, K. et al., 2008. Arc-parallel flow in the mantle wedge beneath Costa Rica and Nicaragua. Nature, 451(7182): 1094-1097.

Hoernle, K. et al., 2011. On- and off-axis chemical heterogeneities along the South Atlantic Mid-Ocean-Ridge (5-11°S): Shallow or deep recycling of ocean crust and/or intraplate volcanism? Earth and Planetary Science Letters, 306(1-2): 86-97.

Hoernle, K. et al., 2000. Existence of complex spatial zonation in the Galápagos plume. Geology, 28(5): 435-438.

Hofmann, A.W., 1988. Chemical differentiation of the Earth: the relationship between mantle, continental crust, and oceanic crust. Earth and Planetary Science Letters, 90(3): 297-314.

Holden, J.C., Dietz, R.S., 1972. Galápagos Gore, NazCoPac Triple Junction and Carnegie/Cocos Ridges. Nature, 235(5336): 266-269.

Ingle, S. et al., 2010. Mechanisms of geochemical and geophysical variations along the western Galápagos Spreading Center. Geochemistry, Geophysics, Geosystems, 11(4): Q04003.

Ito, G., Lin, J., 1995. Oceanic spreading center-hotspot interactions: Constraints from along-isochron bathymetric and gravity anomalies. Geology, 23(7): 657-660.

Ito, G., Lin, J., Graham, D., 2003. Observational and theoretical studies of the dynamics of mantle plume & mid-ocean ridge interaction. Reviews of Geophysics, 41(4): 1017.

Jarosewich, E., Nelen, J.A., Norberg, J.A., 1980. Reference Samples for Electron Microprobe Analysis*. Geostandards Newsletter, 4(1): 43-47.

Jochum, K.P. et al., 2006. MPI-DING reference glasses for in situ microanalysis: New reference values for element concentrations and isotope ratios. Geochemistry, Geophysics, Geosystems, 7(2): Q02008.

Jochum, K.P. et al., 2011. Determination of Reference Values for NIST SRM 610–617 Glasses Following ISO Guidelines. Geostandards and Geoanalytical Research, 35(4): 397-429.

Kincaid, C., Ito, G., Gable, C., 1995. Laboratory investigation of the interaction of off-axis mantle plumes and spreading centres. Nature, 376(6543): 758-761.

Kincaid, C., Schilling, J.G., Gable, C., 1996. The dynamics of off-axis plume-ridge interaction in the uppermost mantle. Earth and Planetary Science Letters, 137(1-4): 29-43.

Klein, E.M., 2003. 3.13 - Geochemistry of the Igneous Oceanic Crust. In: Editors-in-Chief: Heinrich, D.H., Karl, K.T. (Eds.), Treatise on Geochemistry. Pergamon, Oxford, pp. 433-463.

Kokfelt, T.F., Lundstrom, C., Hoernle, K., Hauff, F., Werner, R., 2005. Plume-ridge interaction studied at the Galápagos spreading center: Evidence from 226Ra-230Th-238U and 231Pa-235U isotopic disequilibria. Earth and Planetary Science Letters, 234(1-2): 165-187.

Lanphere, M.A., Dalrymple, G.B., 2000. First-principles calibration of 38Ar tracers: Implications for the ages of 40Ar/39Ar fluence monitors. U.S. Geological Survey Professional Paper(1621): 10.

Le Maitre, R.W. et al., 1989. A classification of igneous rocks and glossary of terms, recommendations of the International Union of Geological Sciences, Subcommission on the Systematics of Igneous Rocks. Blackwell Scientific. Oxford. GB.

Lipman, P.W., Clague, D.A., Moore, J.G., Holcomb, R.T., 1989. South Arch volcanic field-Newly identified young lava flows on the sea floor south of the Hawaiian Ridge. Geology, 17(7): 611-614.

Lohmann, F.C., Hort, M., Phipps Morgan, J., 2009. Flood basalts and ocean island basalts: A deep source or shallow entrainment? Earth and Planetary Science Letters, 284(3-4): 553-563.

Lonsdale, P., 1988. Structural Pattern of the Galápagos Microplate and Evolution of the Galápagos Triple Junctions. Journal of Geophysical Research: Solid Earth, 93(B11): 13551-13574.

Lonsdale, P., 2005. Creation of the Cocos and Nazca plates by fission of the Farallon plate. Tectonophysics, 404(3-4): 237-264.

Lonsdale, P., Klitgord, K.D., 1978. Structure and tectonic history of the eastern Panama Basin. Geological Society of America Bulletin, 89(7): 981-999.

MacDonald, G.A., Katsura, T., 1964. Chemical Composition of Hawaiian Lavas1. Journal of Petrology, 5(1): 82-133.

Meschede, M., Barckhausen, U., 2001. The relationship of the Cocos and Carnegie ridges: age constraints from paleogeographic reconstructions. International Journal of Earth Sciences, 90(2): 386-392.

Montelli, R., Nolet, G., Dahlen, F.A., Masters, G., 2006. A catalogue of deep mantle plumes: New results from finite-frequency tomography. Geochemistry, Geophysics, Geosystems, 7(11): Q11007.

Montelli, R. et al., 2004. Finite-Frequency Tomography Reveals a Variety of Plumes in the Mantle. Science, 303(5656): 338-343.

Morgan, W.J., 1971. Convection Plumes in the Lower Mantle. Nature, 230(5288): 42-43.

Niu, Y.L., Hékinian, R., 2004. Ridge suction drives plume-ridge interactions. In: Hékinian, R., Stoffers, P. (Eds.), Oceanic Hotspots. Springer-Verlag, New York, pp. 285-307.

O'Connor, J.M., Stoffers, P., Wijbrans, J.R., Worthington, T.J., 2007. Migration of widespread long-lived volcanism across the Galápagos Volcanic Province: Evidence for a broad hotspot melting anomaly? Earth and Planetary Science Letters, 263(3-4): 339-354.

Pearce, J.A., 2008. Geochemical fingerprinting of oceanic basalts with applications to ophiolite classification and the search for Archean oceanic crust. Lithos, 100(1-4): 14-48.

Pearce, N.J.G. et al., 1997. A Compilation of New and Published Major and Trace Element Data for NIST SRM 610 and NIST SRM 612 Glass Reference Materials. Geostandards Newsletter, 21(1): 115-144.

Pedersen, R.B., Furnes, H., 2001. Nd- and Pb-isotopic variations through the upper oceanic crust in DSDP/ODP Hole 504B, Costa Rica Rift. Earth and Planetary Science Letters, 189(3-4): 221-235.

Phipps Morgan, J., Morgan, W.J., 1999. Two-stage melting and the geochemical evolution of the mantle: a recipe for mantle plum-pudding. Earth and Planetary Science Letters, 170(3): 215-239.

Phipps Morgan, J., Morgan, W.J., Price, E., 1995. Hotspot melting generates both hotspot volcanism and a hotspot swell? Journal of Geophysical Research: Solid Earth, 100(B5): 8045-8062.

Ribe, N.M., 1996. The dynamics of plume-ridge interaction 2. Off-ridge plumes. Journal of Geophysical Research, 101(B7): 16195-16204.

Ribe, N.M., Christensen, U.R., 1999. The dynamical origin of Hawaiian volcanism. Earth and Planetary Science Letters, 171(4): 517-531.

Ringwood, A.E., 1967. The pyroxene-garnet transformation in the earth's mantle. Earth and Planetary Science Letters, 2(3): 255-263.

Robinson, J.A.C., Wood, B.J., 1998. The depth of the spinel to garnet transition at the peridotite solidus. Earth and Planetary Science Letters, 164(1–2): 277-284.

Rohde, J. et al., 2013. 70 Ma chemical zonation of the Tristan-Gough hotspot track. Geology, 41(3): 335-338.

Sadofsky, S. et al., 2009. Geochemical variations in the Cocos Plate subducting beneath Central America: implications for the composition of arc volcanism and the extent of the Galápagos Hotspot influence on the Cocos oceanic crust. International Journal of Earth Sciences, 98(4): 901-913.

Sallarès, V., Charvis, P., Flueh, E.R., Bialas, J., 2003. Seismic structure of Cocos and Malpelo Volcanic Ridges and implications for hot spot-ridge interaction. Journal of Geophysical Research: Solid Earth, 108(B12): 2564.

Sallarès, V., Charvis, P., Flueh, E.R., Bialas, J., the, S.S.P., 2005. Seismic structure of the Carnegie ridge and the nature of the Galápagos hotspot. Geophysical Journal International, 161(3): 763-788.

Schilling, J.-G., Fontignie, D., Blichert-Toft, J., Kingsley, R., Tomza, U., 2003. Pb-Hf-Nd-Sr isotope variations along the Galápagos Spreading Center (101°-83°W): Constraints on the dispersal of the Galápagos mantle plume. Geochemistry, Geophysics, Geosystems, 4(10): 8512.

Schilling, J.G., Anderson, R.N., Vogt, P., 1976. Rare earth, Fe and Ti variations along the Galápagos spreading centre, and their relationship to the Galápagos mantle plume. Nature, 261(5556): 108-113.

Schilling, J.G., Kingsley, R.H., Devine, J.D., 1982. Galápagos Hot Spot-Spreading Center System 1. Spatial Petrological and Geochemical Variations (83°W–111°W). Journal of Geophysical Research, 87(7): 18.

Sinton, J., Detrick, R., Canales, J.P., Ito, G., Behn, M., 2003. Morphology and segmentation of the western Galápagos Spreading Center, 90.5°-98°W: Plume-ridge interaction at an intermediate spreading ridge. Geochemistry, Geophysics, Geosystems, 4(12): 8515.

Smith, W.H.F., Sandwell, D.T., 1997. Global Sea Floor Topography from Satellite Altimetry and Ship Depth Soundings. Science, 277(5334): 1956-1962.

Sun, S.-s., McDonough, W.F., 1989. Chemical and isotopic systematics of oceanic basalts: implications for mantle composition and processes. Geological Society, London, Special Publications, 42(1): 313-345.

Thompson, R.N., 1974. Primary basalts and magma genesis. Contributions to Mineralogy and Petrology, 45(4): 317-341.

Vogt, P.R., 1976. Plumes, subaxial pipe flow, and topography along the Mid-Oceanic Ridge. Earth and Planetary Science Letters, 29(2): 309-325.

von Huene, R. et al., 1995. Morphotectonics of the Pacific convergent margin of Costa Rica. Geological Society of America Special Papers, 295: 291-308.

Walther, C.H.E., 2003. The crustal structure of the Cocos ridge off Costa Rica. Journal of Geophysical Research: Solid Earth, 108(B3): 2136.

Werner, R., Hoernle, K., Barckhausen, U., Hauff, F., 2003. Geodynamic evolution of the Galápagos hot spot system (Central East Pacific) over the past 20 m.y.: Constraints from morphology, geochemistry, and magnetic anomalies. Geochemistry, Geophysics, Geosystems, 4(12): 1108.

White, W.M., McBirney, A.R., Duncan, R.A., 1993. Petrology and Geochemistry of the Galápagos Islands: Portrait of a Pathological Mantle Plume. Journal of Geophysical Research, 98(B11): 19533-19563.

Wijbrans, J., Németh, K., Martin, U., Balogh, K., 2007. 40Ar/39Ar geochronology of Neogene phreatomagmatic volcanism in the western Pannonian Basin, Hungary. Journal of Volcanology and Geothermal Research, 164(4): 193-204.

Wilson, D.S., 1996. Fastest known spreading on the Miocene Cocos-Pacific Plate Boundary. Geophysical Research Letters, 23(21): 3003-3006.

Wilson, D.S., Hey, R.N., 1995. History of rift propagation and magnetization intensity for the Cocos-Nazca spreading center. Journal of Geophysical Research, 100(B6): 10041-10056.

Yamamoto, M., Morgan, J.P., 2009. North Arch volcanic fields near Hawaii are evidence favouring the restite-root hypothesis for the origin of hotspot swells. Terra Nova, 21(6): 452-466.

Yang, H.-J., Frey, F.A., Clague, D.A., 2003. Constraints on the Source Components of Lavas Forming the Hawaiian North Arch and Honolulu Volcanics. Journal of Petrology, 44(4): 603-627.

Yeo, I.A., Clague, D.A., Martin, J.F., Paduan, J.B., Caress, D.W., 2013. Preeruptive flow focussing in dikes feeding historical pillow ridges on the Juan de Fuca and Gorda Ridges. Geochemistry, Geophysics, Geosystems, 14(9): 3586-3599.

Yoder, H.S., Tilley, C.E., 1962. Origin of Basalt Magmas: An Experimental Study of Natural and Synthetic Rock Systems. Journal of Petrology, 3(3): 342-532.
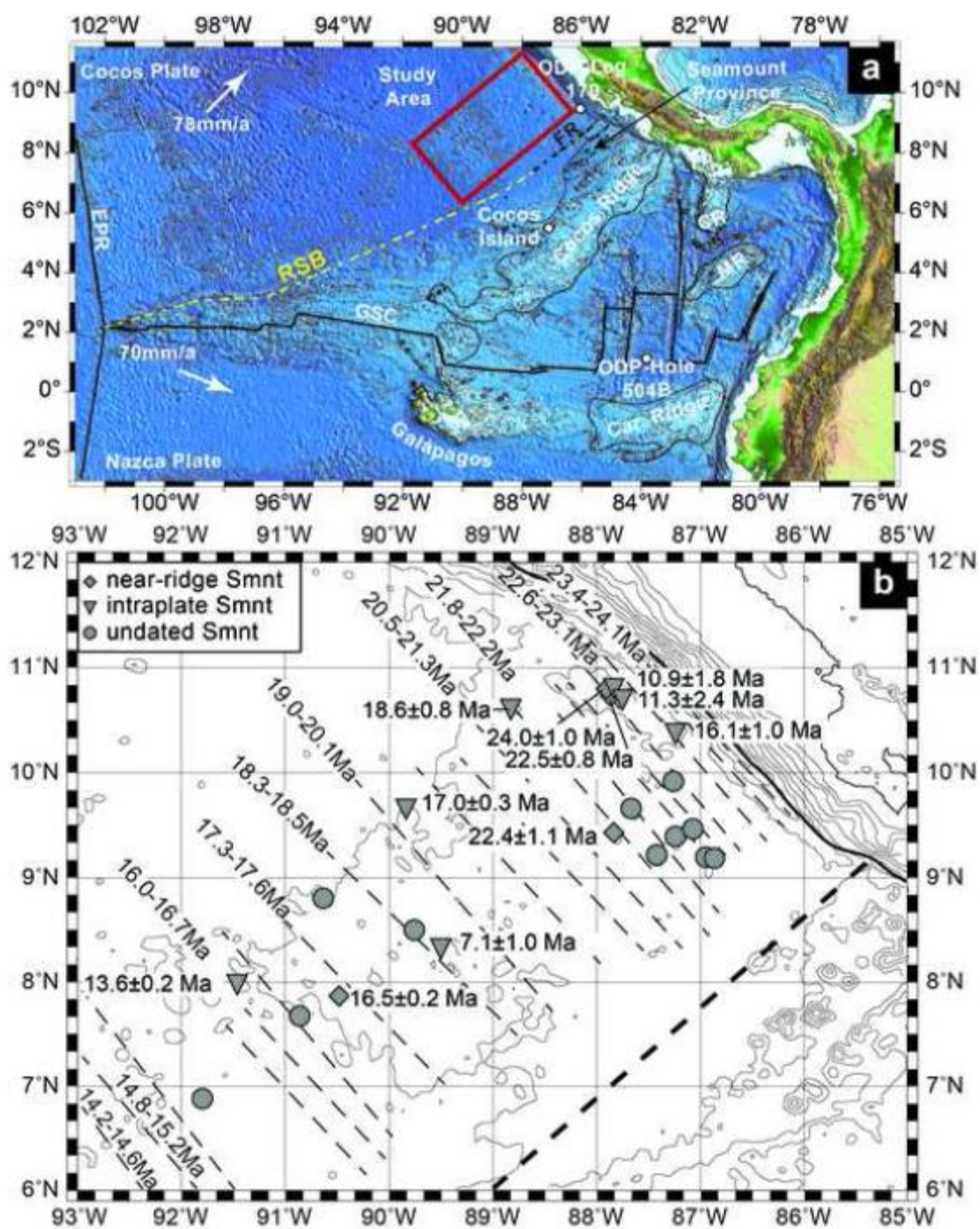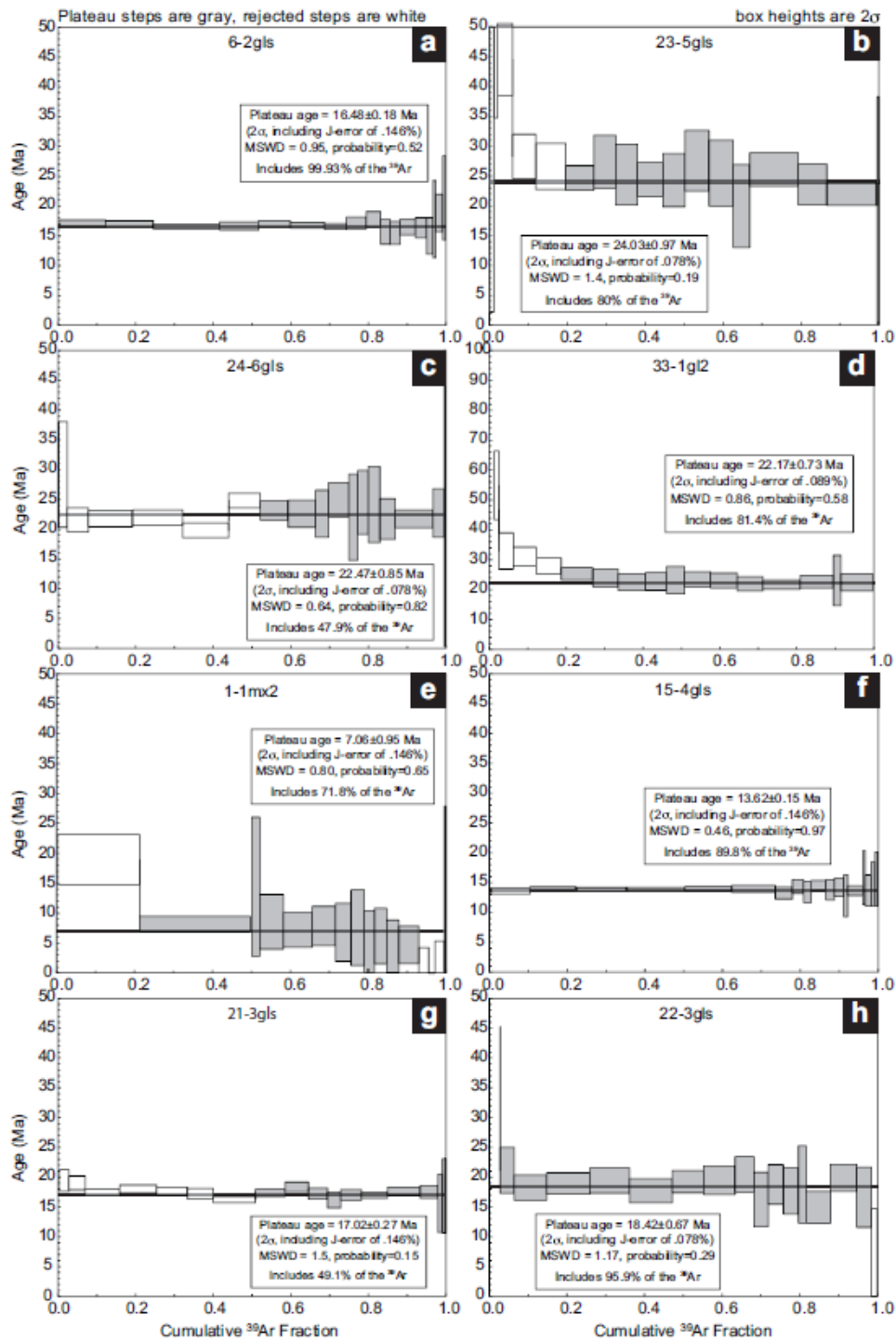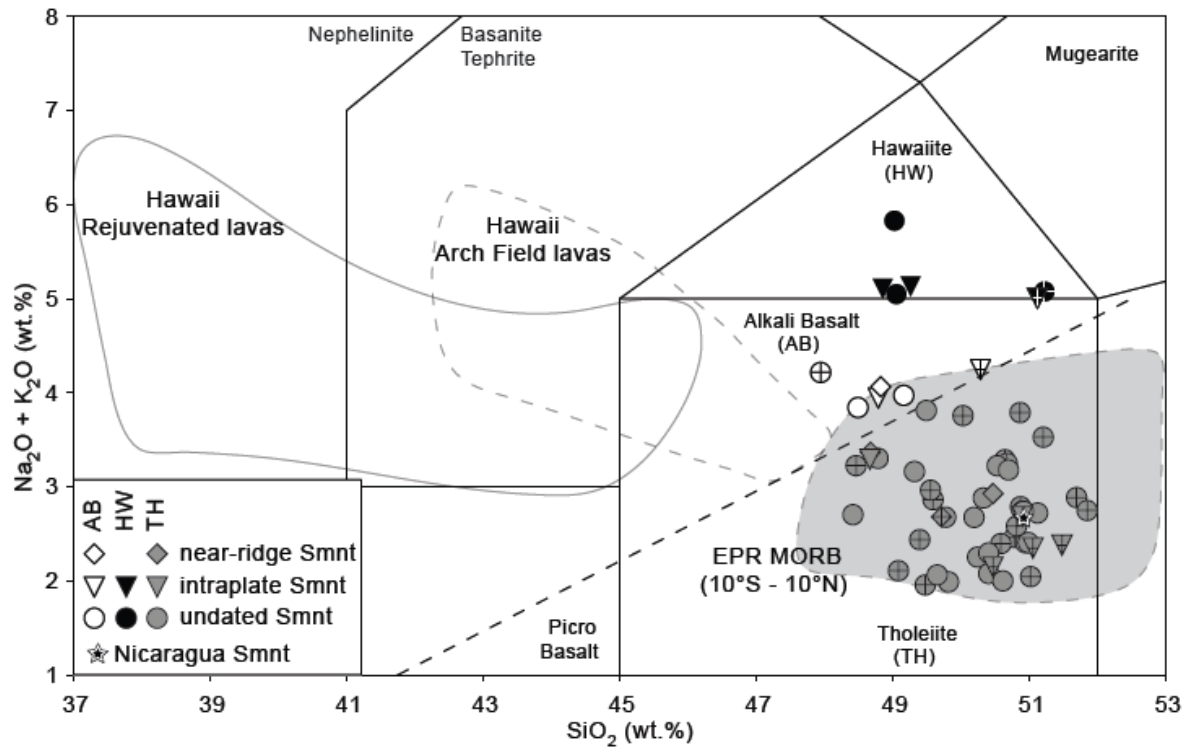
Fig 1

Fig 2

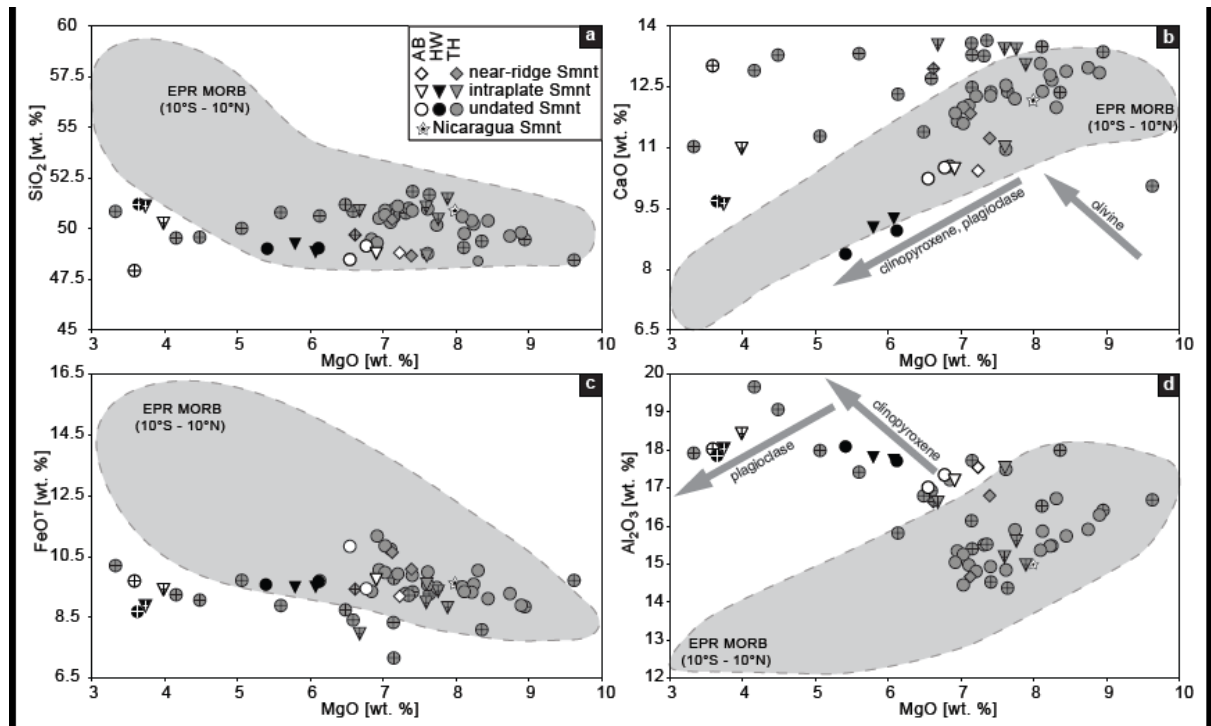Plateau steps are gray, rejected steps are white

box heights are 2σ

a 6-2gls
Plateau age = 16.48±0.18 Ma
(2σ, including J-error of .146%)
MSWD = 0.95, probability=0.52
Includes 99.93% of the ³⁹Ar

b 23-5gls
Plateau age = 24.03±0.97 Ma
(2σ, including J-error of .078%)
MSWD = 1.4, probability=0.19
Includes 80% of the ³⁹Ar

c 24-6gls
Plateau age = 22.47±0.85 Ma
(2σ, including J-error of .078%)
MSWD = 0.64, probability=0.82
Includes 47.9% of the ³⁹Ar

d 33-1gl2
Plateau age = 22.17±0.73 Ma
(2σ, including J-error of .089%)
MSWD = 0.86, probability=0.58
Includes 81.4% of the ³⁹Ar

e 1-1mx2
Plateau age = 7.06±0.95 Ma
(2σ, including J-error of .146%)
MSWD = 0.80, probability=0.65
Includes 71.8% of the ³⁹Ar

f 15-4gls
Plateau age = 13.62±0.15 Ma
(2σ, including J-error of .146%)
MSWD = 0.46, probability=0.97
Includes 89.8% of the ³⁹Ar

g 21-3gls
Plateau age = 17.02±0.27 Ma
(2σ, including J-error of .146%)
MSWD = 1.5, probability=0.15
Includes 49.1% of the ³⁹Ar

h 22-3gls
Plateau age = 18.42±0.67 Ma
(2σ, including J-error of .078%)
MSWD = 1.17, probability=0.29
Includes 95.9% of the ³⁹Ar

Age (Ma)

Cumulative ³⁹Ar Fraction

Fig 3

Fig 4

Fig 5

Fig 6

Fig 7
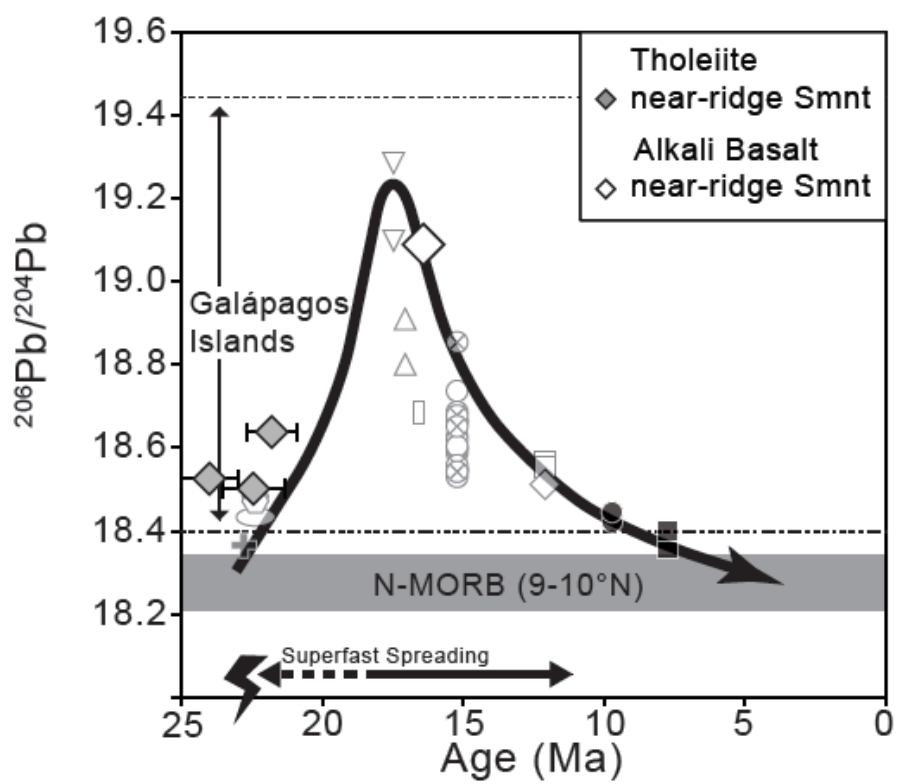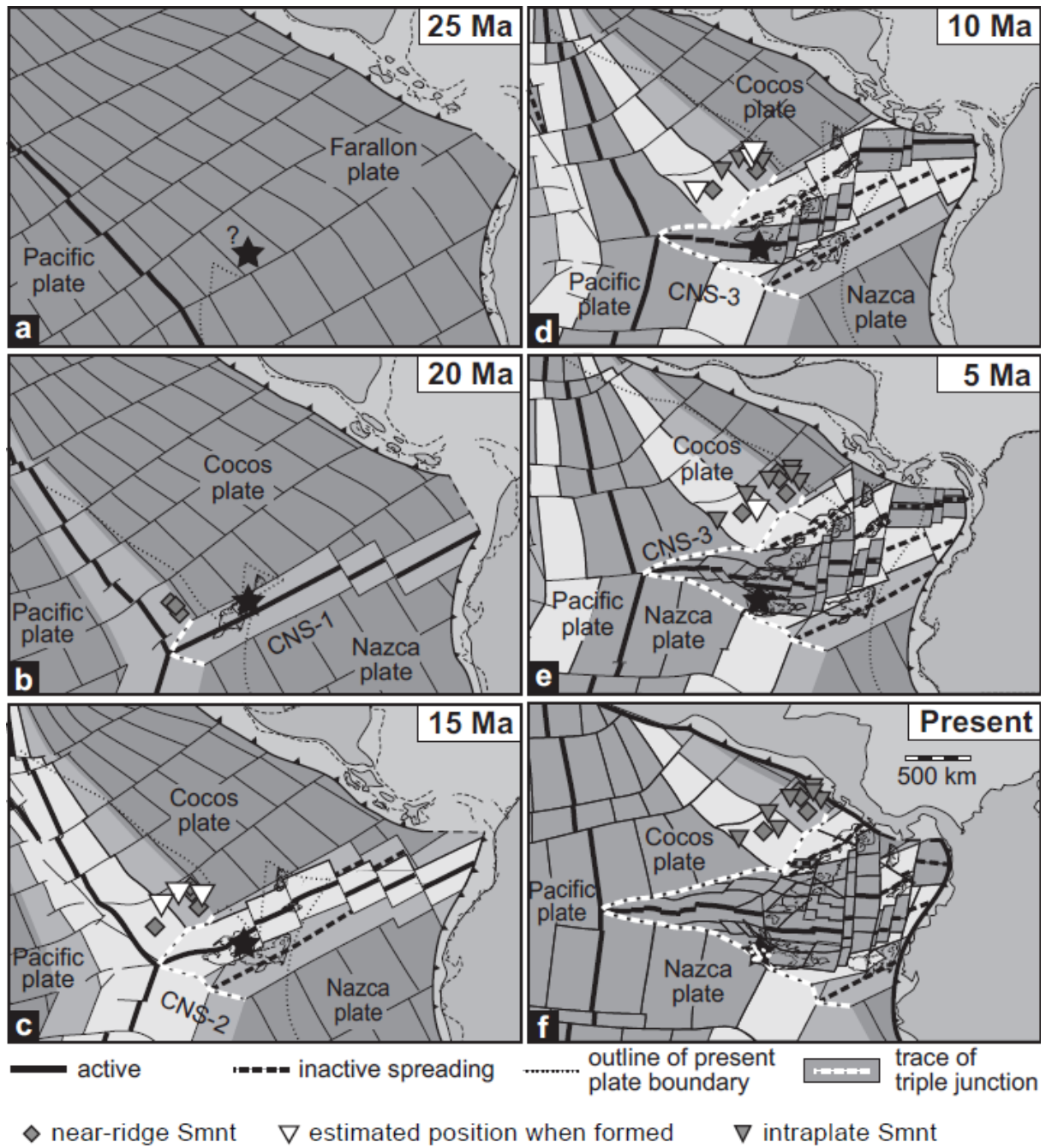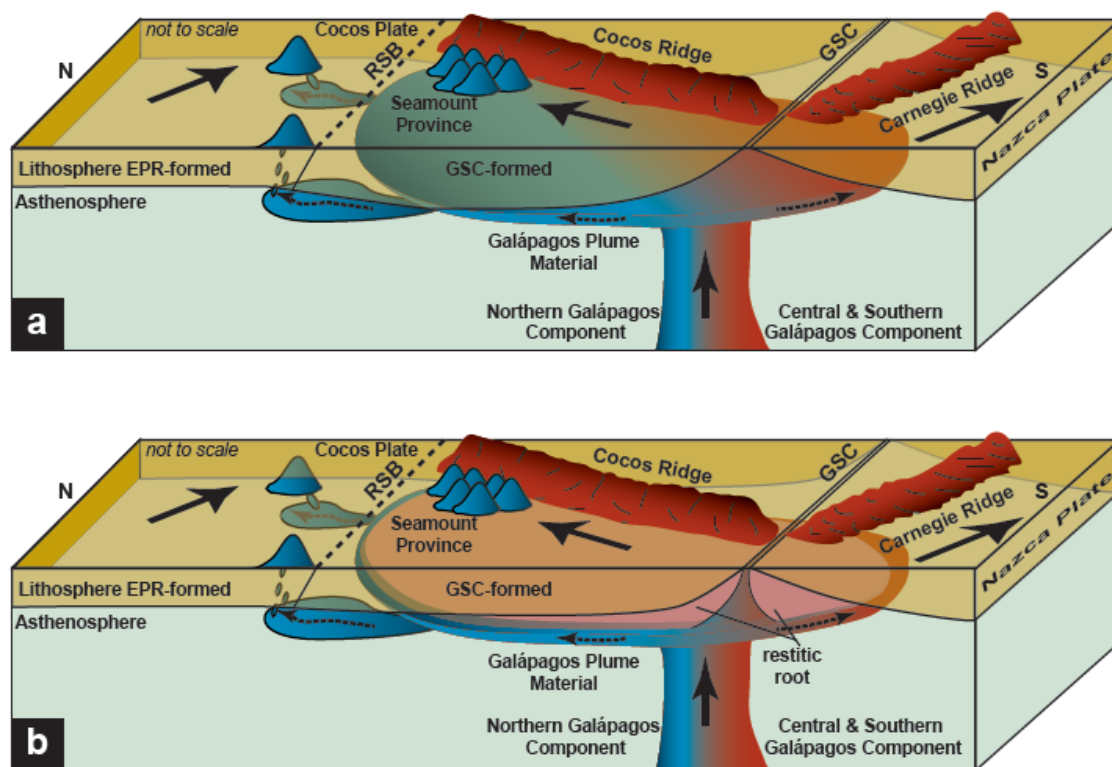
Fig 8

Fig 9

Fig 10

Fig 11

Fig 12

Table 1

Seamount	Sample No. SO208	Analysis ID	Plateau age ± 2SE (Ma)	MSWD	Probability	^{39}Ar %	steps	Plateau step A.I.
PAN-CAKE	DR1-1_wr	1-1mx2	7.1 ± 1.0	0.80	0.65	71.8	2 to 14	<5E-4
GUATBO1	DR6-2	6-2gls	16.5 ± 0.2	0.95	0.52	99.9	2 to 20	<1E-4
SPIEGELEI	DR15-4	15-4gls	13.6 ± 0.2	0.46	0.97	89.8	3 to 20	<1E-4
PICKEL	DR21-3	21-3gls	17.0 ± 0.3	1.50	0.15	49.1	9 to 18	<5E-5
UNNAMED	TVG22-3	22-3gls	18.4 ± 0.7	1.17	0.29	95.9	2 to 16	<5E-5
	TVG22-3	22-3gl2	18.7 ± 0.5	1.20	0.26	65.3	9 to 20	<5E-5
	wtd. Mean	22-3gl	18.6 ± 0.8	0.15	0.70			
BEND FAULT	DR23-5	23-5gls	24 ± 1.0	1.40	0.19	80.0	6 to 16	<5E-5
	DR24-6	24-6gls	22.5 ± 0.9	0.64	0.82	47.9	7 to 20	<5E-5
	DR25-2_wr	25-2mxs	10.0 ± 2.5	1.15	0.29	52.4	2 to 20	<5E-5
	DR25-2_wr	25-2mx2	11.0 ± 0.9	1.30	0.24	65.0	2 to 15	<5E-4
	wtd. Mean	25-2mx	10.9 ± 1.8	0.14	0.71			
LITTLE BEND	DR26-2_wr	26-2mxs	11.3 ± 2.4	1.40	0.12	55.6	2 to 20	<1E-4
SCHRIPPE	DR30-4_wr	30-4mxs	16.1 ± 1.0	0.92	0.55	59.5	2 to 17	<1E-3
KRINGEL	DR33-1	33-1gls	22.7 ± 0.9	1.30	0.23	88.4	4 to 16	<5E-5
	DR33-1	33-1gl2	22.2 ± 0.7	0.86	0.58	81.4	7 to 18	<1E-5
	wtd. Mean	33-1gl	22.4 ± 1.1	0.23	0.63			

MSWD = Mean Squared Weighted Deviates

A.I. = Alteration index = $((36Ar/39Ar) - 0.000268*(37Ar/39Ar))*(J/0.01)/(37Ar/39Ar)$

Table 2

Seamount	Sample No. SO208	rocktype	Lat °N	Long °W	Geomagnetic Polarity Timescale Interval, Ma		Chron	Ar/Ar Dating Age Ma	± 2SE (M)	Differenz Ma	
					min	max				min	max
Near-ridge Seamount Samples											
EGG	DR6-2	Alkali Basalt	7.84	90.47	17.3	17.6	5D	16.5	0.2	0.8	1.1
BEND FAULT	DR23-5	Tholeiite	10.77	87.89	22.6	24.1	6B - 6C	24.0	1.0	-1.4	0.1
	DR23-5_wr	Tholeiite	10.77	87.89	22.6	24.1	6B - 6C				
	DR24-6	Tholeiite	10.76	87.87	22.6	24.1	6B - 6C	22.5	0.9	0.1	1.6
KRINGEL	DR33-1	Tholeiite	9.41	87.84	21.8	21.9	6AA	22.4 *	1.1	-0.6	-0.5
	DR33-1_wr	Tholeiite	9.41	87.84	21.8	21.9	6AA				
Intraplate Seamount Samples											
PAN-CAKE	DR1-1_wr	Tholeiite	8.22	89.51	18.3	18.8	5E	7.1	1.0	11.2	11.7
SPIEGELEI	DR15-4	Hawaiite	7.95	91.47	16.0	16.7	5C	13.6	0.2	2.4	3.1
	DR15-4_wr	Hawaiite	7.95	91.47	16.0	16.7	5C				
PICKEL	DR21-3	Alkali Basalt	9.63	89.84	19.0	20.1	6	17.0	0.3	2.0	3.1
	DR21-3_wr	Alkali Basalt	9.63	89.84	19.0	20.1	6				
UNNAMED	TVG22-3	Tholeiite	10.59	88.83	21.8	21.9	6AA	18.6 *	0.8	3.2	3.3
BEND FAULT	DR25-2	Tholeiite	10.79	87.84	22.6	24.1	6B - 6C				
	DR25-2_wr	Tholeiite	10.79	87.84	22.6	24.1	6B - 6C	10.9 *	1.8	11.7	13.2
LITTLE BEND	DR26-2_wr	Tholeiite	10.69	87.76	22.6	24.1	6B - 6C	11.3	2.4	11.3	12.8
SCHRIPPE	DR30-4_wr	Tholeiite	10.41	87.25	23.4	24.1	6C	16.1	1.0	7.3	8.0
Undated Seamounts Samples											
PAN-CAKE	DR1-5	Tholeiite	8.22	89.51	18.3	18.8	6e				
HALF-MOON	DR2-1_wr	Tholeiite	8.47	89.76	18.3	18.8	5E				
BOXER	DR7-2_wr	Tholeiite	7.64	90.87	16.0	16.7	5C				
HORSESHOE	DR9-5_wr	Tholeiite	6.90	91.59	14.8	16.7	5B - 5C				
SPIEGELEI	DR15-5	Hawaiite	7.95	91.47	16.0	16.7	5C				
	DR15-6_wr	Hawaiite	7.95	91.47	16.0	16.7	5C				
EYE	DR17-1	Tholeiite	8.75	90.72	17.3	18.8	5D - 5E				
	DR17-	Tholeiite	8.75	90.7	17.	18.	5D -				

	1_wr	e		2	3	8	5E
	DR17-7	Tholeiite	8.75	90.72	17.3	18.8	5D - 5E
	DR17-19	Tholeiite	8.75	90.72	17.3	18.8	5D - 5E
	DR17-20	Tholeiite	8.75	90.72	17.3	18.8	5D - 5E
PICKEL	DR21-1	Alkali Basalt	9.63	89.84	19.0	20.1	6
	DR21-2	Tholeiite	9.63	89.84	19.0	20.1	6
UNNAMED	TVG22-1	Tholeiite	10.59	88.83	21.8	21.9	6AA
	TVG22-4_wr	Tholeiite	10.59	88.83	21.8	21.9	6AA
BEND FAULT	DR23-1_wr	Tholeiite	10.77	87.89	22.6	24.1	6B - 6C
	DR23-6	Tholeiite	10.77	87.89	22.6	24.1	6B - 6C
	DR24-2_wr	Tholeiite	10.76	87.87	22.6	24.1	6B - 6C
	DR24-20_wr	Tholeiite	10.76	87.87	22.6	24.1	6B - 6C
	DR25-4	Tholeiite	10.79	87.84	22.6	24.1	6B - 6C
	DR25-10_wr	Tholeiite	10.79	87.84	22.6	24.1	6B - 6C
LITTLE BEND	DR26-3	Tholeiite	10.69	87.76	22.6	24.1	6B - 6C
SCHRIPPE	DR30-1	Alkali Basalt	10.41	87.25	23.4	24.1	6C
	DR30-1_wr	Tholeiite	10.41	87.25	23.4	24.1	6C
	DR30-2	Hawaiite	10.41	87.25	23.4	24.1	6C
AMMONIT	DR31-1	Tholeiite	9.90	87.27	22.6	23.1	6B
	DR31-2	Tholeiite	9.90	87.27	22.6	23.1	6B
	DR31-2_wr	Tholeiite	9.90	87.27	22.6	23.1	6B
	DR31-3_wr	Tholeiite	9.90	87.27	22.6	23.1	6B
GUARDIAN	DR32-1	Tholeiite	9.64	87.68	22.2	22.3	6AA1
	DR32-2_wr	Tholeiite	9.64	87.68	22.2	22.3	6AA2
	DR32-6_wr	Tholeiite	9.64	87.68	22.2	22.3	6AA3
BAGEL	DR36-1_wr	Tholeiite	9.14	87.42	21.8	22.3	6AA - 6AA1
OJO	DR37-1_wr	Tholeiite	9.37	87.25	22.6	23.1	6B
	DR37-3_wr	Tholeiite	9.37	87.25	22.6	23.1	6B
ZECKE	DR38-1	Tholeiite	9.45	87.08	22.6	23.1	6B
	DR38-2	Tholeiite	9.45	87.08	22.6	23.1	6B
	DR38-4_wr	Tholeiite	9.45	87.08	22.6	23.1	6B

HOOK	DR39-1_wr	Tholeiite	9.14	86.94	22.6	23.1	6B
	DR39-2_wr	Tholeiite	9.14	86.94	22.6	23.1	6B
	DR39-8-VC	Tholeiite	9.14	86.94	22.6	23.1	6B
	DR39-9-VC	Tholeiite	9.14	86.94	22.6	23.1	6B
	DR40-1_wr	Tholeiite	9.15	86.92	22.6	23.1	6B

Cocos Plate Seamounts offshore NW Costa Rica and SW Nicaragua: Implications for large-scale distribution of Galápagos plume material in the upper mantle

Antje Herbrich[1]*, Kaj Hoernle[1], Reinhard Werner[1], Folkmar Hauff[1], Paul v.d. Boogard[1], Dieter Garbe-Schönberg[2]

[1] GEOMAR Helmholtz Centre for Ocean Research Kiel, Wischhofstraße 1-3, D-24148 Kiel, Germany

[2] Institute of Geosciences, University of Kiel, Ludewig-Meyn-Strasse 10, D-24118 Kiel, Germany

Highlights

- Ages and geochemistry of 19 seamounts on the EPR-formed Cocos Plate crust determined.

- Seamounts formed off axis and within plate, distant to Galápagos plume.

- A mixture of plume-like material with two different depleted sources is required.

- Seamounts manifest large-scale transport of plume material.

- Variable lithospheric thickness and/or restitic root cause decompression melting.